

1

2 **Persistent ocean anomalies as a response to northern hemisphere heating**

3 **induced by biomass burning variability**

4

5 Ryohei Yamaguchi^a, Ji-Eun Kim^{b,c}, Keith B. Rodgers^{b,c}, Karl Stein^{b,c}, Axel Timmermann^{b,c},

6 Sun-Seon Lee^{b,c}, Lei Huang^d, Malte F. Stuecker^e, John T. Fasullo^f, Gokhan Danabasoglu^f,

7 Clara Deser^f, Jean-Francois Lamarque^f, Nan A. Rosenbloom^f, Jim Edwards^f

8 ^a *Research Institute for Global Change, Japan Agency for Marine-Earth Science and Technology, Yokosuka,*
9 *Japan*

10 ^b *Center for Climate Physics, Institute for Basic Science, Busan, South Korea*

11 ^c *Pusan National University, Busan, South Korea*

12 ^d *College of Resource Environment and Tourism, Capital Normal University, China*

13 ^e *Department of Oceanography and International Pacific Research Center, School of Ocean and Earth Science*
14 *and Technology, University of Hawai‘i at Mānoa, Honolulu, HI, USA*

15 ^f *Climate and Global Dynamics Laboratory, National Center for Atmospheric Research, Boulder,*
16 *CO, USA*

17

18

19 *Corresponding author:* Ryohei Yamaguchi, ryamaguchi@jamstec.go.jp

20

21

ABSTRACT

22 Biomass burning aerosol (BBA) emissions in the Coupled Model Intercomparison Project
23 phase 6 (CMIP6) historical forcing fields have enhanced temporal variability during the years
24 1997–2014, due to the inclusion of satellite records. Recent studies document that the
25 corresponding inhomogeneous shortwave forcing can cause changes in permafrost, soil
26 moisture, clouds, which contribute to a net terrestrial northern hemisphere warming, relative to
27 earlier periods. Here, we investigate the ocean response to the associated hemispherically
28 asymmetric warming using two 50-member ensemble simulations conducted with the
29 Community Earth System Model version 2 Large Ensemble forced by different BBA emissions
30 (CMIP6 default and temporally smoothed over 1990–2020). Differences between the two sub-
31 ensemble means show that ocean temperature anomalies occur during periods of high BBA
32 variability and subsequently persist over multiple decades. In the North Atlantic, surface
33 warming is efficiently compensated for by decreased northward oceanic heat transport due to
34 a slowdown of the Atlantic Meridional Overturning Circulation. In the North Pacific, surface
35 warming is compensated for by an anomalous cross-equatorial cell (CEC) that reduces
36 northward oceanic heat transport. The heat that converges in the South Pacific through the
37 anomalous CEC is shunted into the subsurface and contributes to formation of long-lasting
38 ocean temperature anomalies. The anomalous CEC is maintained through latitude-dependent
39 contributions from narrow western boundary currents and basin-wide near-surface Ekman
40 transport. These results indicate that interannual variability in forcing fields may significantly
41 change the long time-scale climate background state, presenting a potential uncertainty in
42 CMIP6-class climate projections forced without interannual variability.

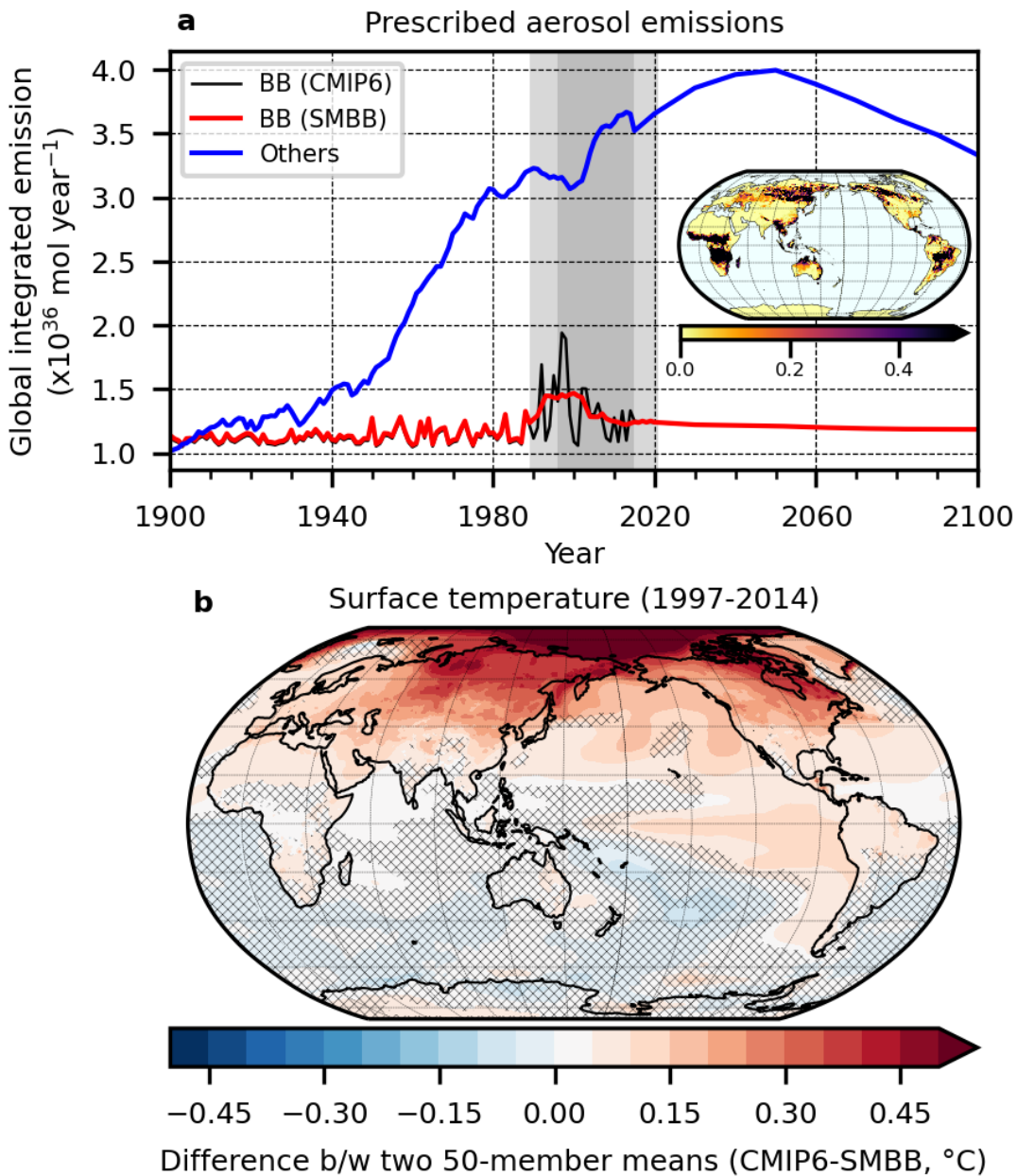
43

44

45 **1. Introduction**

46 Aerosol forcings in the latest Coupled Model Intercomparison Project Phase 6 (CMIP6,
47 Eyring et al. 2016) protocol include contributions from biomass burning aerosol (BBA)
48 emissions and a variety of other anthropogenic aerosol emissions (including fluxes from
49 industrial activities and land/marine transport, etc.) in addition to natural emissions (dimethyl
50 sulfide, biogenic aerosols, etc.). Although the total amount of global BBA emissions over the
51 recent historical period is smaller than other anthropogenic emissions ([Fig. 1a](#)), the year-to-
52 year variability of BBA emissions is relatively large. Fires, the main source of BBA emissions,
53 have a spatially heterogenous distribution and temporal variations caused by changes in
54 vegetation productivity, human activity, climate, and interactions between them (Archibald et
55 al. 2013; van der Werf et al. 2017). BBA emissions forcing data in CMIP6 (BB4CMIP6, van
56 Marle et al. 2017), spanning 1750 to the present, are based on a multi-model mean flux
57 estimated from the Fire Model Intercomparison Project (FireMIP, Rabin et al. 2017). Satellite-
58 derived observational products derived [Global Fire Emissions Database version 4s (GFED4s),
59 for 1997 onwards], charcoal datasets (in temperate and boreal regions), and visibility records
60 (in the Arc of deforestation and Equatorial Asia from the 1960s to 1997) are also incorporated
61 in the BB4CMIP6 (van Marle et al. 2017). The use of observational data which are only
62 available over recent decades, in particular over the satellite era (1997 onwards), provides more
63 globally realistic emissions data but also result in inhomogeneities in the amplitude of temporal
64 variability that are a spurious consequence of patching together disparate types of historical
65 reconstructions ([Fig. 5](#) in van Marle et al. 2017). Variability in BBA emissions is greater during
66 the recent period when large-scale observations are more directly incorporated into the
67 products ([Fig. 1a](#)), although the net amount (long-term mean) of the BBA emissions does not
68 vary dramatically over time. The spurious change in the amplitude of interannual BBA
69 emissions is a new feature of CMIP6 forcing that was not present in CMIP5, in which decadal
70 mean fluxes were used to construct BBA emissions (Lamarque et al. 2010).

71



72

73 Fig. 1. (a) Globally integrated CMIP6 aerosol emissions forcings from biomass burning
 74 (BB, black) and other anthropogenic sources (blue). Temporally smoothed BB emissions over
 75 the period of the large temporal variability (1990–2020, light gray-shaded period) used in this
 76 study are superimposed as a red line [BB (SMBB)]. The dark gray-shaded period is when the
 77 satellite (GFED4s) observed data were used (1997–2014). The inserted map shows BB
 78 (CMIP6) aerosol emission climatology for 1990–2020 (10^{11} mol cm 2 s $^{-1}$). (b) Surface
 79 (radiative) temperature differences between two sub-ensemble means of a 50-member set
 80 forced by BB (CMIP6) and another 50-member set forced by BB (SMBB) from the Community
 81 Earth System Model 2 Large Ensemble simulations. Statistically insignificant differences at
 82 the 95% confidence level are cross-hatched. See the details of the experimental settings and
 83 the statistical tests in Section 2.

84

Several recent studies have shown that high-amplitude interannual variability in BBA emissions can affect not only climate variability for model-simulated fields, but also their longer-timescale variability and mean state. This effect is manifested for instance in 2-m air temperature (Fasullo et al. 2022; Kim et al. *under review*), Arctic sea ice (DeRepentigny et al. 2022), as well as the global hydrological cycle (Heyblom et al. 2022). In particular, in the high-latitude Northern Hemisphere (NH), where there are many sources of BBA emissions (Fig. 1a), an increase in BBA emissions variability from 1997 onwards causes a net thinning of clouds, thereby enhancing incident shortwave radiation, which in turn warms the surface in the NH (Fasullo et al. 2022). The interannual temperature fluctuations generated by the anomalous satellite-era BBA variability can be further rectified into a long-term terrestrial warming through permafrost melting and soil moisture changes (Fig. 1b and Kim et al. *under review*). As the NH warming expands widely beyond the localized sources of anomalous BBA emissions, it induces anomalous Arctic sea ice loss in CMIP6 historical simulations that was absent in CMIP5 simulations (DeRepentigny et al. 2022). In turn these processes can further contribute to shifts in the global-scale hydrological cycle (Heyblom et al. 2022).

It is generally known that hemispherically asymmetric radiative forcing (provided through changes in orbital forcing, albedo, aerosol forcing, or other drivers) leads to interhemispheric thermal gradients, and the coupled ocean-atmosphere system works to reduce these gradient (see the reviews by Chiang and Friedman 2012; Schneider et al. 2014; Kang 2020). In the atmosphere, anomalous interhemispheric thermal gradients lead to compensating cross-equatorial heat transport (CEHT) by Hadley circulation adjustments and corresponding meridional shifts of the Intertropical Convergence Zone (ITCZ) (Broccoli et al. 2006; Kang et al. 2008). As for the ocean, compensating CEHT is supplied by anomalies in meridional overturning circulation (MOC) and/or anomalies in the shallow subtropical cell structures that are partly coupled to perturbations in the atmospheric Hadley Cell (Green and Marshall 2017; Schneider 2017; Kang et al. 2018). A number of studies since the early 1980s have improved our understanding of the global response to asymmetric forcing. However the role of the ocean in determining the global response remains relatively unexplored (Kang 2020), despite the fact that its importance is well recognized (e.g., Deser et al. 2015; Yoshimori et al. 2018; Kang et al. 2021).

The objective of this study is to identify and understand how the anomalous year-to-year BBA CMIP6 forcing translates into anomalous ocean signals that persist beyond interannual

timescales. Our study complements the work of Kim et al. (*under review*), which focuses on the mechanisms that support shorter-timescale rectified land surface responses (warming) over the NH. As with the study of Kim et al. (*under review*), we use output from the Community Earth System Model version 2 Large Ensemble simulations (CESM2-LE, Rodgers et al. 2021). The 100-ensemble-member CESM2-LE is comprised of two sets of 50 ensemble member experiments, integrated from 1850 to 2100 with the CMIP6 Historical (1850–2014) and the Shared Socio-economic Pathway 3-7.0 (SSP3-7.0) (2015–2100) scenarios with different BBA forcings. For the BBA forcing, the first 50 members are forced with the default CMIP6 BBA forcing (BB4CMIP6), and the remaining 50 members use temporally smoothed BB4CMIP6 for the period of high-amplitude interannual variability (1990–2020) (Fig 1a, details in Section 2). By taking ensemble mean averages across each 50-member sub-ensemble and differencing the resulting ensemble means, one can deconvolve the forced rectified response and associated uncertainty due to background variability. Comparison of the two sets of sub-ensemble averages reveals the presence of ocean anomalies that are induced by the large BBA emissions variability. The ocean temperature anomalies persist over several decades beyond the period of divergent BBA forcing, as well as for the previously reported NH atmospheric warming and Arctic sea ice melting (see Section 3 for details).

After describing the details of the model experimental design and the statistical methods used in this study in Section 2, we show comparisons of the two sub-ensemble mean fields and the atmosphere-ocean responses to the decadal NH warming from the perspective of the energy budget in Section 3. In section 4, we provide a mechanistic account of the ocean's role in compensating for the interhemispheric thermal gradient set by the high-amplitude interannual variability of the BBA forcing. The results are summarized along with a discussion of implications in Section 5.

141

142 **2. Data and methods**

143 We use output from the 100-member LE conducted using CESM2 (Danabasoglu et al. 144 2020). CESM2 is a CMIP6-generation Earth System Model developed by the U.S. National 145 Center for Atmospheric Research (NCAR) in collaboration with the broader community. It 146 comprises of the Community Atmosphere Model version 6 (CAM6, Bogenschutz et al. 2018), 147 the Community Land Model version 5 (CLM5, Lawrence et al. 2019), the Parallel Ocean

148 Program version 2 (POP2, Smith et al. 2010; Danabasoglu et al. 2012), and the Community Ice
149 Code version 5 (CICE5, Hunke et al. 2015). CAM6 has a resolution of 1.25° in longitude and
150 0.9° in latitude with 32 vertical levels. CLM5 has the same horizontal grid as CAM6. POP2
151 and CICE5 share the same horizontal grid, with a uniform spacing of 1.125° in the zonal
152 direction and varying in the meridional direction from 0.65° at high- and mid-latitudes to 0.25°
153 at the Equator, with 60 vertical levels (20 of these are in the upper 200 m of the water column).

154 Initial conditions for the 100-member LE, conducted as part of a collaboration between the
155 IBS Center for Climate Physics and the CESM group at NCAR, are a mixture of “macro-” and
156 “micro-” perturbation initializations (Rodgers et al. 2021). Twenty macro-perturbation initial
157 conditions were selected at 10-year intervals from starting points at least 1,000 years into the
158 CESM2 pre-industrial simulation (Danabasoglu et al. 2020). By adding small round-off level
159 perturbations to the atmospheric potential temperature field, 20 micro-perturbation initial
160 conditions were created from each of the additional four macro-perturbation initial conditions
161 (4 x 20 micro-perturbation initial conditions). The four additional macro-initial states were
162 chosen based on conditions of the Atlantic Meridional Overturning Circulation (AMOC) (see
163 Rodgers et al. 2021 for details). All members were integrated from 1850 to 2100 with common
164 forcings from the CMIP6 Historical forcings for the period from 1850 to 2014 and the SSP3-
165 7.0 scenario for the later period, except for the BBA forcing. Any climate state differences
166 among members originating from differences in the initial conditions are negligible for the
167 period of interest in this study (1990–onward, i.e., 140 years after the initialization). Indeed,
168 the initial condition dependence of the AMOC, which could have a relatively long memory,
169 drops below the detection limit within a few decades (Rodgers et al. 2021, their Fig. S2).

170 The 100-member LE is comprised of two sub-ensembles of 50 members each, with each
171 sub-ensemble distinguished by its BBA forcing over 1990–2020 ([Fig. 1a](#)). The first 50
172 members are compliant with CMIP6 forcing protocols, thereby including the high-amplitude
173 BBA emissions variability, with this sub-ensemble henceforth referred to as CMIP6. The
174 second group of 50 members uses temporally-smoothed CMIP6 BBA forcing over the period
175 1990–2020 ([Fig. 1a](#)) and is henceforth referred to as SMBB. The temporal smoothing was
176 performed with an 11-year moving average applied separately for each month of the monthly
177 averaged time series to preserve the seasonal cycle. We emphasize that as a simple moving
178 average was applied, the net integrated BBA emissions over the period of interest are nearly
179 conserved between the two forcings. In addition to the difference in BBA forcing, some slight

180 corrections of forcings and code modifications, mainly in CLM5, were applied for the 50
181 SMBB members (see Section 2.4 in Rodgers et al. 2021 for details). The impacts from these
182 additional modifications are rather minor with no apparent effects on the climate mean state.
183 For the purposes of this study, we base our interpretation on the assumption that the differences
184 between the two sub-ensemble means after year 1990 can be attributed mainly to the
185 differences in the temporal variability of BBA between the two sub-ensembles over 1990–2020.

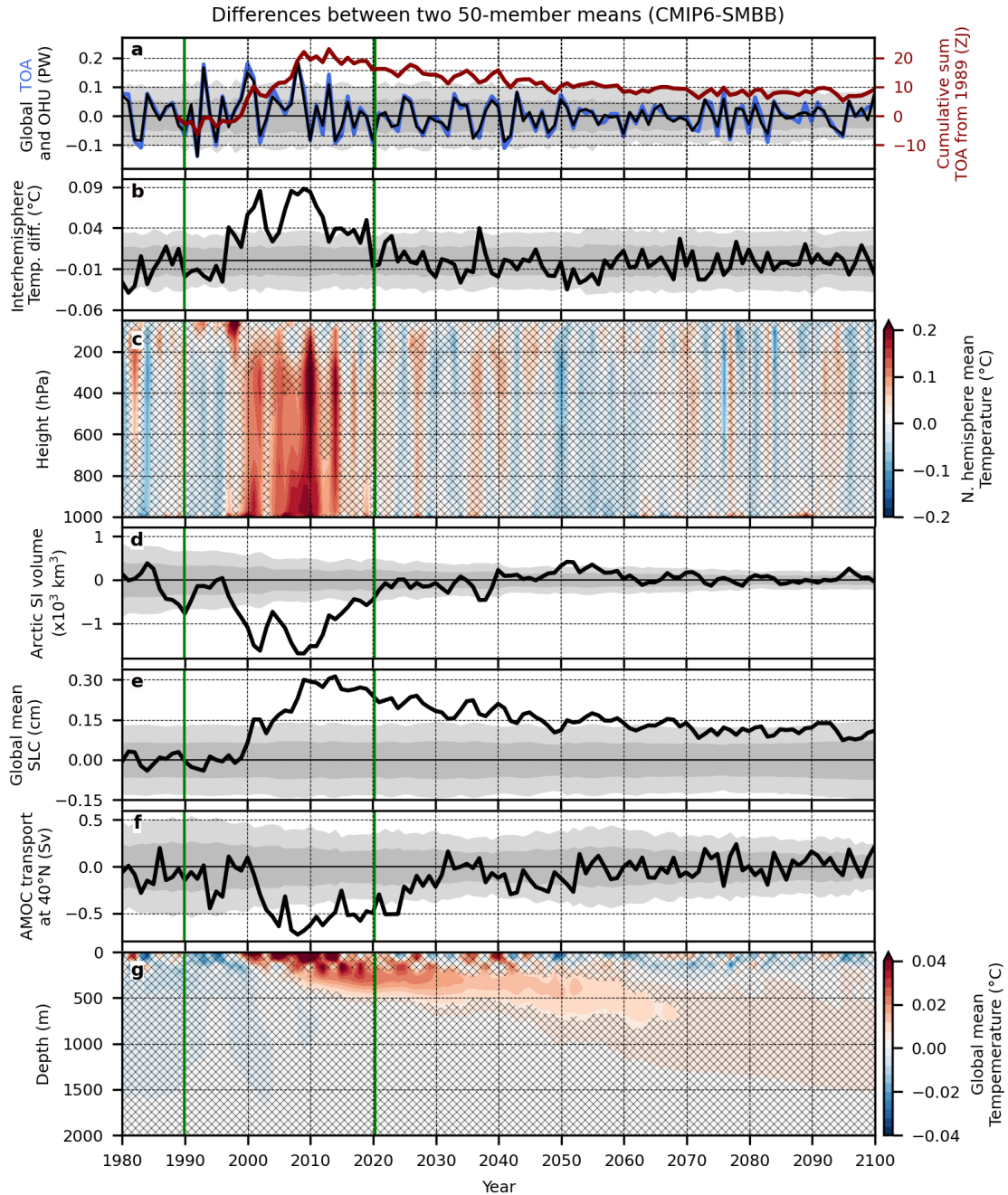
186 To determine if a difference between sub-ensemble means is statistically significant, we
187 use a bootstrap-like method to utilize information on background internal variability which can
188 be estimated from the LE members. We first randomly select two groups of 50 members from
189 the 100-member LE and compute the difference between the means of the two groups.
190 Repeating the computation 10,000 times, we calculate the standard deviation of the 10,000
191 differences, with the mean converging to zero as the number of trials increases. For the case
192 where the difference between the CMIP6 50-member mean and SMBB 50-member mean
193 (referred to as the 50-50 difference) is outside the range of twice the standard deviation, the
194 50-50 difference is defined as statistically significant at the 95% confidence level, i.e., it is not
195 likely to occur by chance due to the background internal variability.

196

197 **3. Impacts of high-amplitude interannual variability in BBA emissions**

198 *a. Anomalous heat entered into the Earth System*

199



200

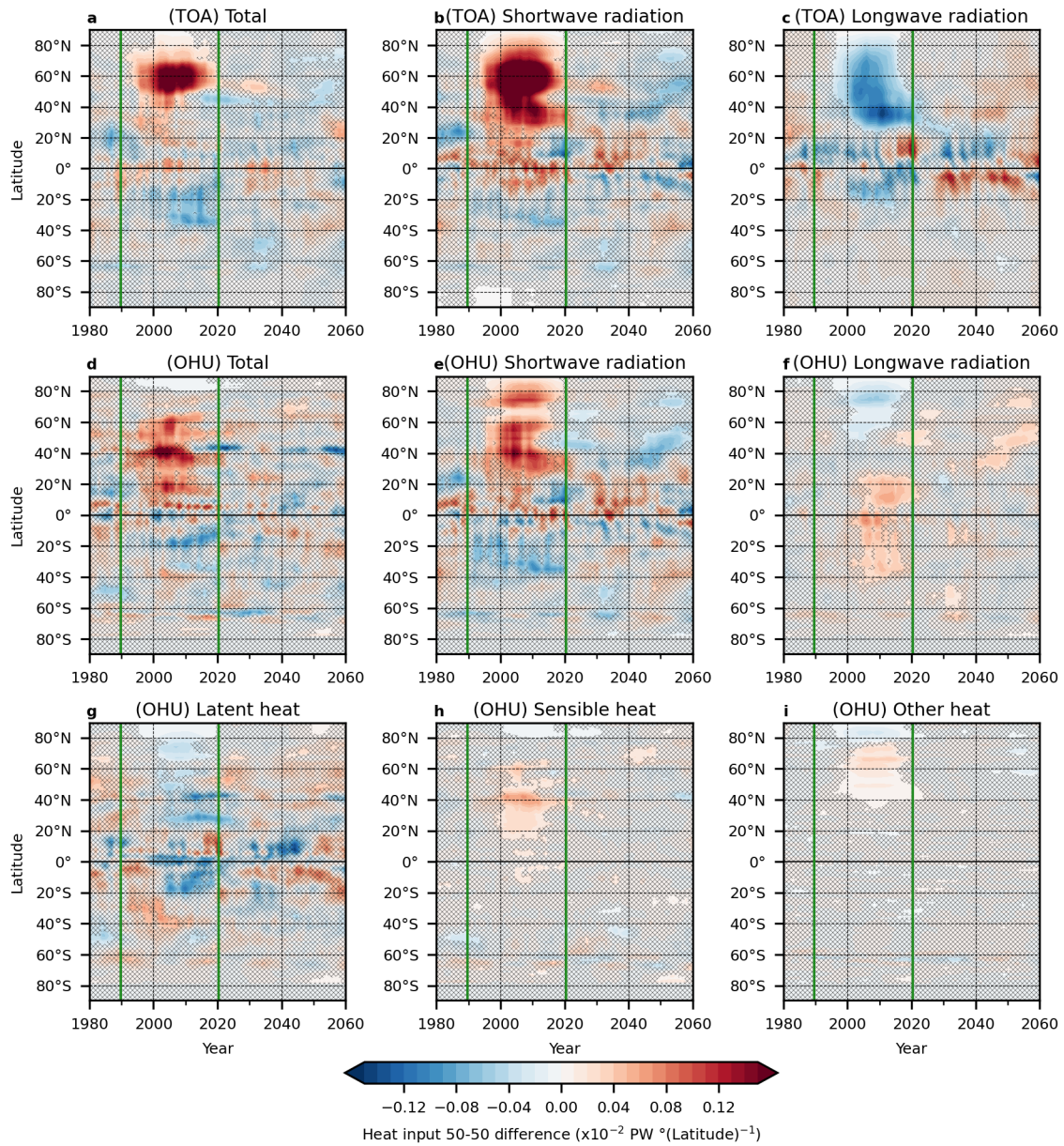
201 Fig. 2. The difference in sub-ensemble means between the 50-member CMIP6 and 50-
 202 member SMBB simulations for (a) globally integrated top of atmosphere radiation imbalance
 203 (TOA, blue line) and ocean heat uptake (OHU i.e., net ocean surface heat flux, black line), (b)
 204 interhemispheric difference in column-mean atmospheric temperature (Northern Hemisphere
 205 minus Southern Hemisphere), (c) Northern Hemisphere mean atmospheric temperature profiles,
 206 (d) Arctic sea ice (SI) volume, (e) global mean steric sea level change (SLC, estimated from
 207 sea water density changes), (f) AMOC maximum transport at 40°N , and (g) global mean ocean
 208 temperature profiles. In (a), the cumulative sum of TOA difference from 1989 (red line with
 209 right axis) is also shown. The time interval surrounded by two green lines corresponds to the
 210 time interval where CMIP6 and SMBB forcings differ. The estimated range of standard
 211 deviations (σ) based on the bootstrapping analysis are shown in (a), (b), and (d-f) (light gray

212 shadings for $\pm \sigma$ and dark gray shadings for $\pm 2\sigma$). Statistically insignificant differences at
213 the 95% confidence level are cross-hatched in (c) and (g).

214

215 Statistically significant CMIP6 vs. SMBB differences in several climatological metrics are
216 seen during and/or beyond the period of different BBA forcing (1990–2020) in Fig. 2. In terms
217 of the global energy budget, a relative excess of heat enters the Earth system in the form of
218 radiative fluxes through the top of the atmosphere (TOA, up to 0.4 W m^{-2} as an annual mean)
219 in the CMIP6 members (blue line in Fig. 2a). The total amount of heat accumulated from the
220 beginning of the period with different forcing reaches up to 20 ZJ (red line in Fig. 2a). The
221 anomalous heat input from the top of the atmosphere enters as an anomalous shortwave
222 radiative flux, mainly within the NH high latitudes (Figs. 3a–3c, and Fig. 4a). The heat that
223 enters the Earth system serves to immediately warm the atmosphere (Fasullo et al. 2022) and
224 to melt Arctic sea ice (DeRepentigny et al. 2022) through the rectified decadal NH warming
225 (Kim et al. *under review*) (Figs. 2c and 2d). In contrast to the rapidity with which the heat enters
226 the system, it is radiated back to space rather slowly (red line in Fig. 2a). Whereas the heat
227 largely enters the Earth system in the NH high latitudes, with a maximum spanning from
228 Siberia to North America (Fig. 4a), the regions of anomalous emissions back to space as
229 longwave radiation over 2015–2030 occur principally on the eastern flanks of the North Pacific
230 and North Atlantic Oceans (Fig. 4b).

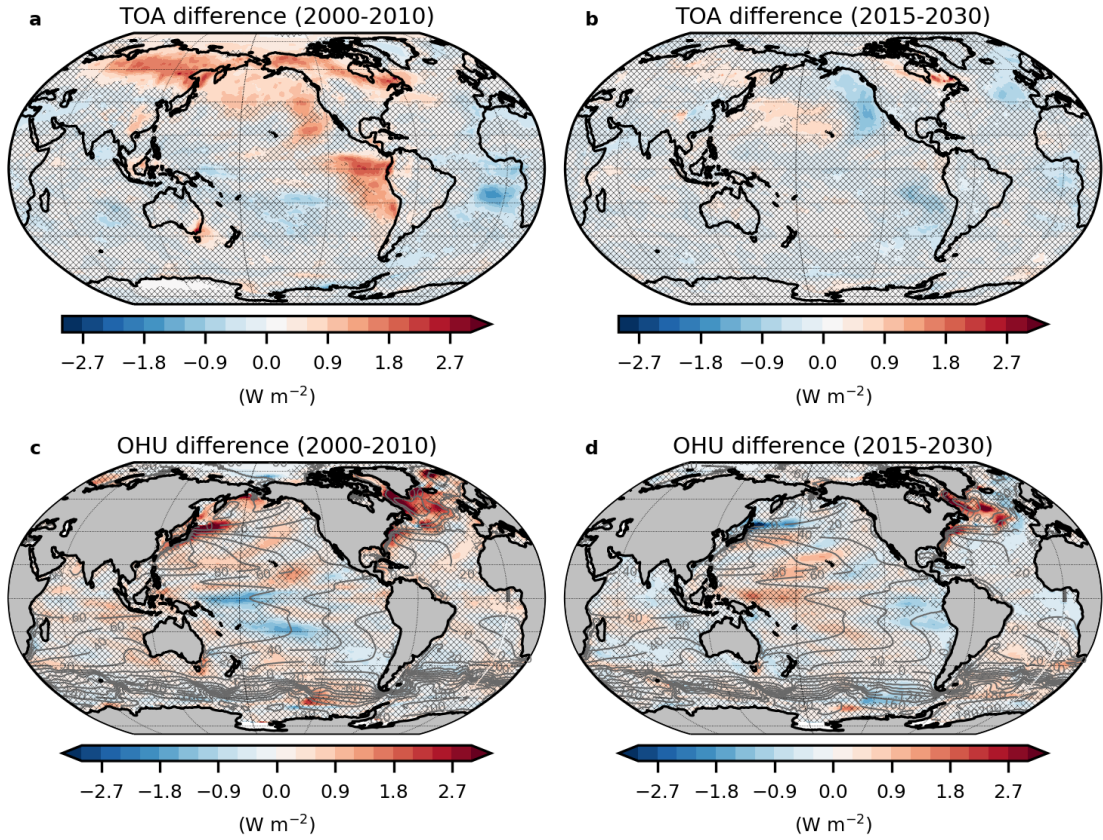
231



232

233 Fig. 3. The difference in CMIP6 (50 members) and SMBB (50 members) ensemble means
 234 of zonally-integrated (a–c) top of atmosphere radiation imbalance (TOA) and (d–i) ocean heat
 235 uptake (OHU). TOA consists of shortwave radiation (b) and longwave radiation (c)
 236 components and the modeled OHU is decomposed into components of shortwave radiation (e),
 237 longwave radiation (f), latent heat of evaporation (g), sensible heat (h), and other heat from sea
 238 ice process and river runoff (i). 11-year running mean is applied for all panels. Positive
 239 differences indicate anomalous downward flux (TOA: to the atmosphere, OHU: to the ocean)
 240 in CMIP6 members. The time interval between the two green lines corresponds to when CMIP6
 241 and SMBB forcings are different (1990–2020). Statistically insignificant signals at the 95%
 242 confidence level are cross-hatched.

243



244

245 Fig. 4. Differences in top of atmosphere radiation imbalance (TOA)
 246 and ocean heat uptake (OHU) fluxes between the CMIP6 and SMBB sub-ensemble means.
 247 Spatial patterns are shown
 248 for the periods of absorbing heat (2000–2010, a and c) and releasing heat (2015–2030, b and
 249 d), defined based on the global mean TOA flux differences (Fig. 2a). Positive differences
 250 indicate anomalous downward fluxes (TOA: to the atmosphere, OHU: to the ocean) in CMIP6
 251 relative SMBB. 100-member ensemble mean climatologies of sea surface height [SSH (cm)]
 252 for each period are superimposed in (c) and (d). Statistically insignificant differences at the
 253 95% confidence level are cross-hatched.

253

254 Less than 10% of the total anomalous heat input during 1990–2020 goes to warm the
 255 atmosphere and melt sea ice. The vast majority of the anomalous heat (~92%) is absorbed by
 256 the oceans (black line in Fig 2a). Preferential ocean heat uptake (OHU, i.e., net air-sea surface
 257 heat flux) regions include the band represented by the NH trade winds (near 20°N), winter deep
 258 convection regions near the western boundary currents (WBCs) in both the North Pacific and
 259 Atlantic, and along the Arctic sea ice margin (around 60°N) where sea ice retreats and hence
 260 heat exchange is enhanced (Figs. 3d and 4c). Shortwave radiative flux anomalies are the main
 261 contributors to anomalous ocean heat uptake (Figs. 3d–3i) in the NH high-latitude. The heat
 262 taken up by the ocean raises the global mean ocean temperature between the surface and ~700
 263 m depth (Fig. 2g) and expands the ocean, as can be seen with the global mean steric sea level

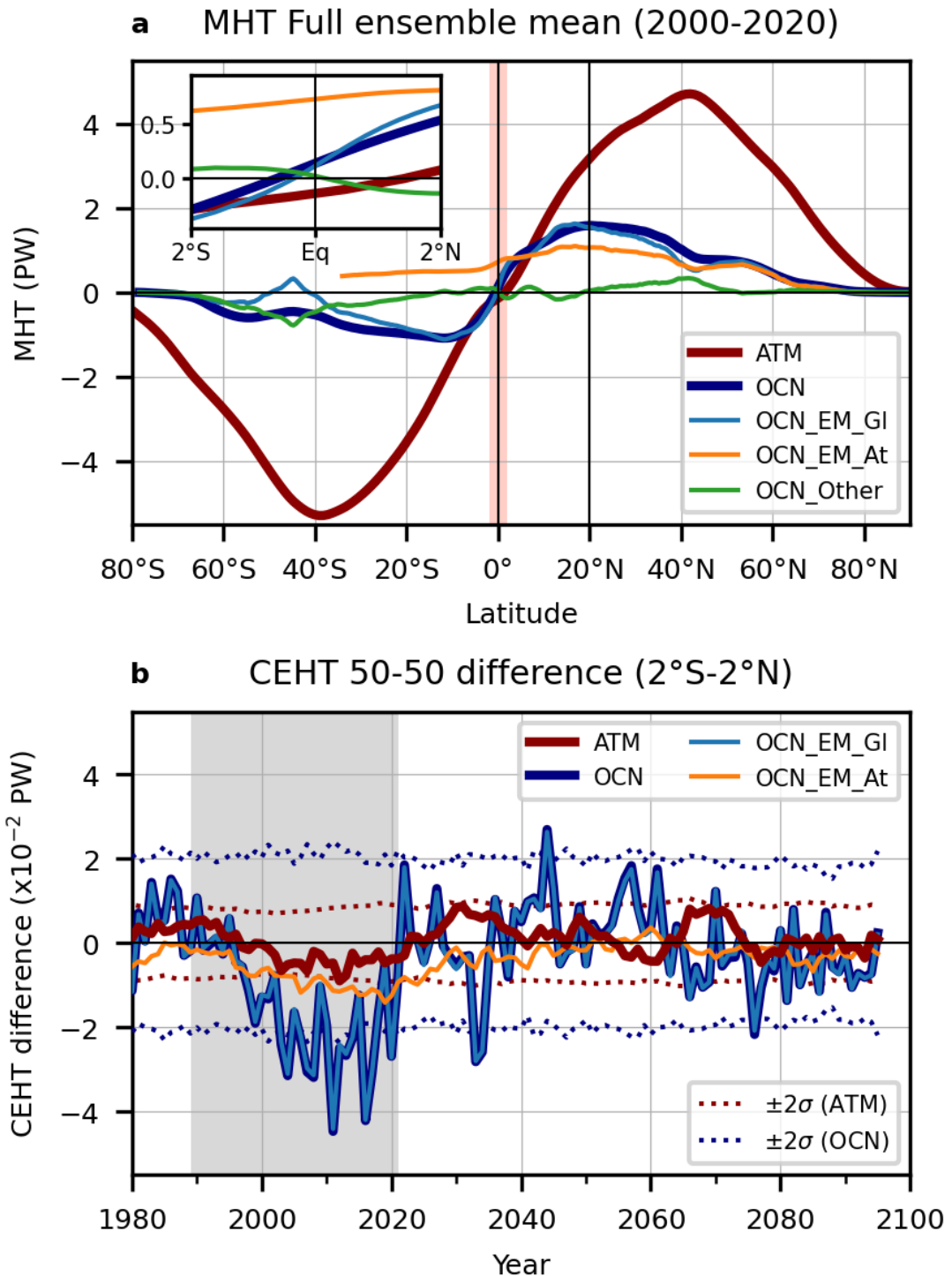
264 change of 3 mm ([Fig. 2e](#)). Previously reported atmospheric and cryosphere anomalies induced
265 by the high-amplitude BBA emissions (Fasullo et al. 2022; DeRepentigny et al. 2022; Kim et
266 al. *under review*) disappear soon after the end of the period where CMIP6 and SMBB forcings
267 are divergent (e.g., [Figs. 2c](#) and [2d](#)). In contrast, oceanic anomalies remain in the system for at
268 least several decades, acting as a longer-term memory in the system (e.g., [Figs. 2e–2g](#)). In the
269 next section, we investigate the mechanisms responsible for generating these long-lasting
270 ocean anomalies by tracking ocean heat anomalies within the ocean interior.

271

272 *b. Change in atmospheric and oceanic interhemispheric heat transport*

273 Increases in the interhemispheric thermal gradient ([Fig. 2b](#)) due to hemispherically
274 asymmetric warming anomalies lead to coordinated adjustments of the atmosphere and ocean
275 meridional heat transports (MHTs) that act to reduce the gradient, as has been documented in
276 previous studies (e.g., Deser et al. 2015; Green and Marshall 2017; Kang et al. 2021). For our
277 case, where the ocean transports heat northward and the atmosphere transports heat southward
278 across the equator under climatological conditions ([Fig. 5a, inlay figure](#)), the NH decadal
279 warming anomaly induced by high-amplitude variability in BBA emissions reduces the
280 northward ocean heat transport and increases the southward atmospheric heat transport at the
281 equator ([Fig. 5b](#)). As a result, the excess heat added to the NH is compensated or transported
282 to the Southern Hemisphere (SH), thus contributing to decreasing the interhemispheric thermal
283 gradient. Changes in the atmospheric CEHT are linked to changes in the Hadley circulation
284 (Kang et al. 2008; Schneider et al. 2014), which is further manifested by the meridional shift
285 of the ITCZ. Also in the present case, a northward shift of the ITCZ is clearly identified in the
286 Atlantic and Indian Ocean sectors ([Fig. S1b](#)). Changes in the wind-driven component of the
287 ocean CEHT are coupled via the trade winds to changes in the Hadley circulation (Green and
288 Marshall 2017), and for this case the ocean CEHT anomaly occurs in the same direction
289 (southward) as those in the atmosphere.

290



291

292 Fig. 5. (a) 100-member ensemble mean climatology (2000–2020) of the meridional heat
 293 transport (MHT, positive northward) by the atmosphere (ATM) and ocean (OCN). The ocean
 294 MHT is decomposed into the Eulerian mean circulation component (OCN_EM) and other
 295 components (OCN_Other) including the mesoscale eddy (bolus) transport, horizontal diffusion,
 296 and parameterized sub-mesoscale transport. The Eulerian component in the Atlantic
 297 (OCN_EM_At) is shown separately from the Eulerian component over the global domain
 298 (OCN_EM_Gl). The inserted panel in (a) shows an enlarged view of the climatological MHTs

299 near the equator. (b) Differences in cross-equatorial heat transport (CEHT) between CMIP6
300 and SMBB sub-ensemble means. Note that the OCN and OCN_EM_Gl lines in (b) almost
301 overlap each other. An 11-year running mean is applied to the time series. The gray shaded
302 period corresponds to when CMIP6 and SMBB forcings are different (1990–2020). The
303 estimated two standard deviations ranges ($\pm 2\sigma$) based on the bootstrapping are shown as
304 dashed lines.

305

306 Responses of the oceanic and atmospheric CEHT to interhemispheric forcings are sensitive
307 to the geographical location and intensity of the forcings (Hawcroft et al. 2018; White et al.
308 2018; Yu and Pritchard 2019). In the present case, the magnitude of the CEHT anomaly is
309 approximately five times larger in the ocean than that in the atmosphere, with no phase
310 difference between the two (Fig. 5b). The southward ocean CEHT anomalies are mostly
311 induced by the contribution from the Eulerian mean (EM) currents, and the other components
312 [mesoscale eddy (bolus) transport, horizontal diffusion, and parameterized sub-mesoscale
313 transport] do not contribute strongly. For the climatological mean behavior of CESM2, CEHT
314 for the Atlantic Ocean is positive (northward heat transport) and CEHT for the Indo-Pacific
315 domain (OC_EM_Gl minus OCN_EM_At in Fig. 5a) is negative (southward heat transport).
316 However, the directions of the BBA-induced CEHT anomalies are southward in both ocean
317 basins. Of the southward ocean CEHT anomaly, 40% occurs in the Atlantic, and the remaining
318 60% in the Indo-Pacific (Fig. 5b), with this result standing in contrast to a previous study that
319 emphasized the Atlantic contribution under the NH cooling (Yu and Pritchard 2019).

320

321 **4. Mechanisms for the long-lasting ocean anomalies**

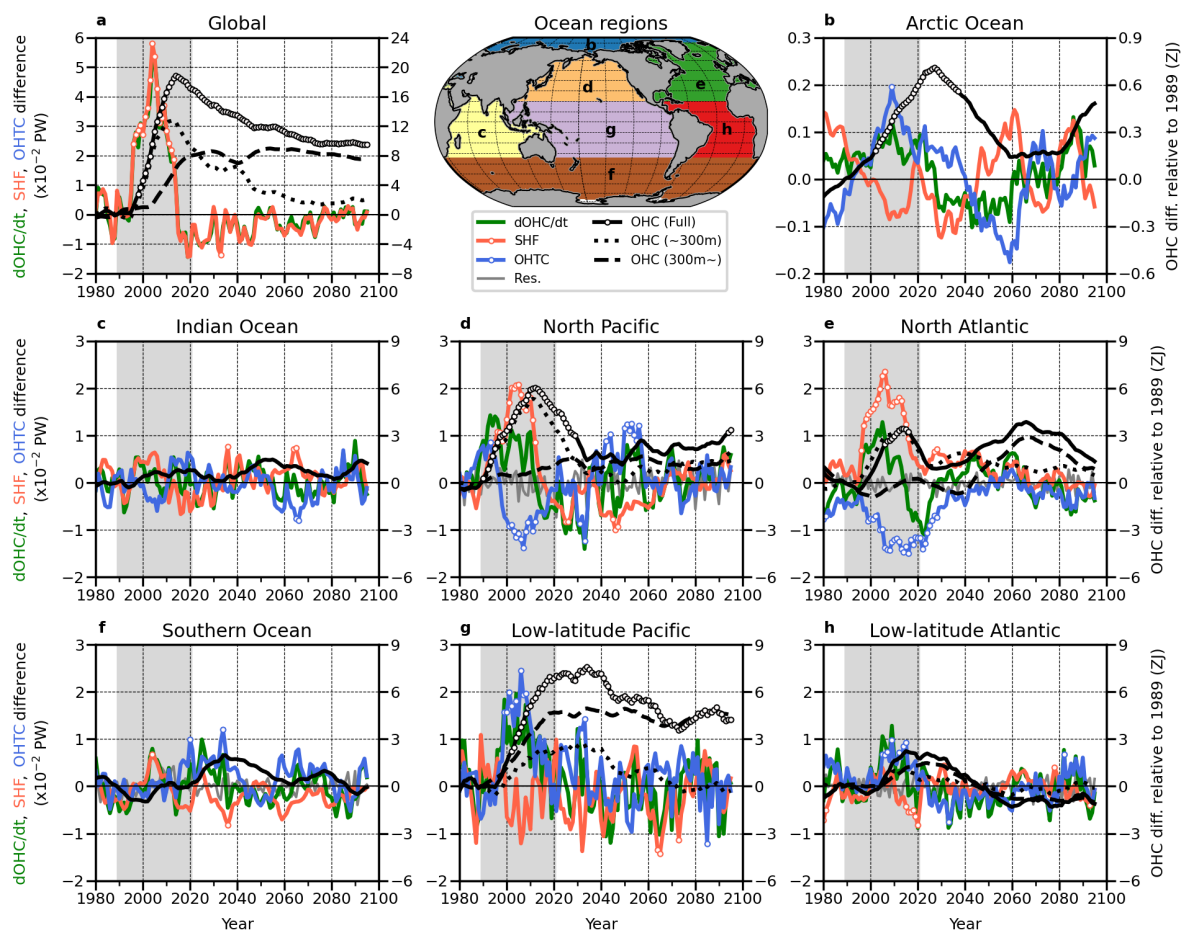
322 *a. Fate of heat taken up by ocean*

323 The fate of the heat absorbed by the ocean is identified by applying a budget analysis for
324 ocean heat content (OHC) (Fig. 6). For each basin, changes in ocean heat content ($dOHC/dt$,
325 green lines in Fig. 6) should be balanced by the sum of the air-sea heat flux at surface (SHF,
326 orange lines in Fig. 6) and the ocean heat transport convergence (OHTC, blue lines in Fig. 6).
327 It should be noted that the OHTCs are estimated directly from temperature and velocity fields
328 only for those basins where the relevant model output was saved (only for the North Pacific,
329 North Atlantic, Southern Ocean, and Low-latitude Atlantic); otherwise, they are estimated as a
330 residual in the budget analysis. For the full global ocean domain (Fig. 6a, no OHTC term exists
331 by definition), during the period of the high-amplitude variability in BBA emissions (1990–

15

332 2020), ocean heating of $\sim 6 \times 10^{-2}$ PW occurs, resulting in up to 18 ZJ of anomalous OHC in the
 333 CMIP6 members. Subsequently, the global OHC anomaly decreases more slowly than its
 334 increase. Although the pattern of ocean heat loss is less coherent than it is for ocean heat uptake,
 335 relatively strong heat release can be identified along the Kuroshio/Oyashio extension region
 336 and in the eastern Tropical and South Pacific (Fig. 4d). These are due to decreases in incoming
 337 shortwave radiation and anomalous latent heat fluxes, respectively (Figs. 3d–3i). While the
 338 ocean steadily loses heat after the end of the period, the global OHC anomaly remains
 339 statistically significant at the 95% confidence level until the end of the simulation (year 2100)
 340 in association with accumulation of heat below 300 m depth (Fig. 6a).

341



342

343 Fig. 6. Budgets for the ocean heat content differences between the sub-ensemble means of
 344 CMIP6 and SMBB members. For (a) the global ocean and for (b–h) each ocean basin (its spatial
 345 map is inserted as the upper central panel), changes in the 50–50 differences in the full-depth
 346 ocean heat content ($dOHC/dt$), the sea surface heat flux (SHF), and the ocean heat transport
 347 convergence (OHTC) are shown as green, orange, and blue lines with the left y-axis,
 348 respectively. The residuals (Res.) are also shown as gray lines with the left y-axis if available.
 349 Black solid lines are 50–50 differences in the full-depth OHC (with the right y-axis). In the

350 panels for global (a), Pacific (d and g), and Atlantic (e and h), 50–50 differences in OHCs above
351 300 m and below 300 m are also shown as dotted and dashed lines with the right y-axis,
352 respectively. The Southern Ocean is defined as oceans south of 34°S, and the Pacific and
353 Atlantic are separated into their respective northern and low-latitude parts at 20°N. An 11-year
354 running mean is applied to all timeseries. The white dots on the black, blue, and orange lines
355 indicate statistically significant differences at the 95% confidence level based on the
356 bootstrapping method. The gray-shaded period corresponds to the time interval where CMIP6
357 and SMBB forcing are different (1990–2020).

358

359 The North Pacific ([Fig. 6d](#)) and North Atlantic ([Fig. 6e](#)), where anomalous surface heating
360 due to anomalous BBA forcing is the largest, show seemingly similar responses. Surface
361 heating in the North Pacific and North Atlantic reaches up to 2×10^{-2} PW during the time of
362 high-amplitude BBA emissions variability, resulting in a corresponding local increase in OHC
363 (~ approximately year 2016). In both regions, the negative OHTC anomalies (divergence of
364 ocean heat transport) following the anomalous positive SHF perturbations dominate the
365 dOHC/dt. The OHC anomalies themselves return to a statistically insignificant level by the
366 year 2020 for the North Atlantic and by the year 2030 for the North Pacific, although the
367 negative SHF anomalies also partially contribute to the OHC decrease in the North Pacific.
368 Contemporaneously with the negative OHTC anomalies in the North Atlantic (~ year 2040),
369 the OHC in the Arctic Ocean is significantly increased by the positive OHTC anomaly ([Fig.](#)
370 [6b](#)). On the other hand, positive OHTC anomalies in the low-latitude Atlantic (~ year 2020)
371 are subsequently offset by the negative SHF anomalies, and therefore OHC anomalies do not
372 increase to a statistically significant level ([Fig. 6h](#)). Positive OHTC anomalies in the low-
373 latitude Pacific, which occur at the same time as negative OHTC anomalies in the North Pacific
374 (in approximately years 2000–2010), cause positive OHC anomalies which are the only
375 statistically significant OHC anomalies among ocean regions at the end of the simulation ([Fig.](#)
376 [6g](#)). The long-lasting low-latitude Pacific OHC anomalies are largely confined to the
377 subsurface (deeper than 300 m) and account for the largest fraction (50%) of the remaining
378 global OHC anomalies at the end of the simulation.

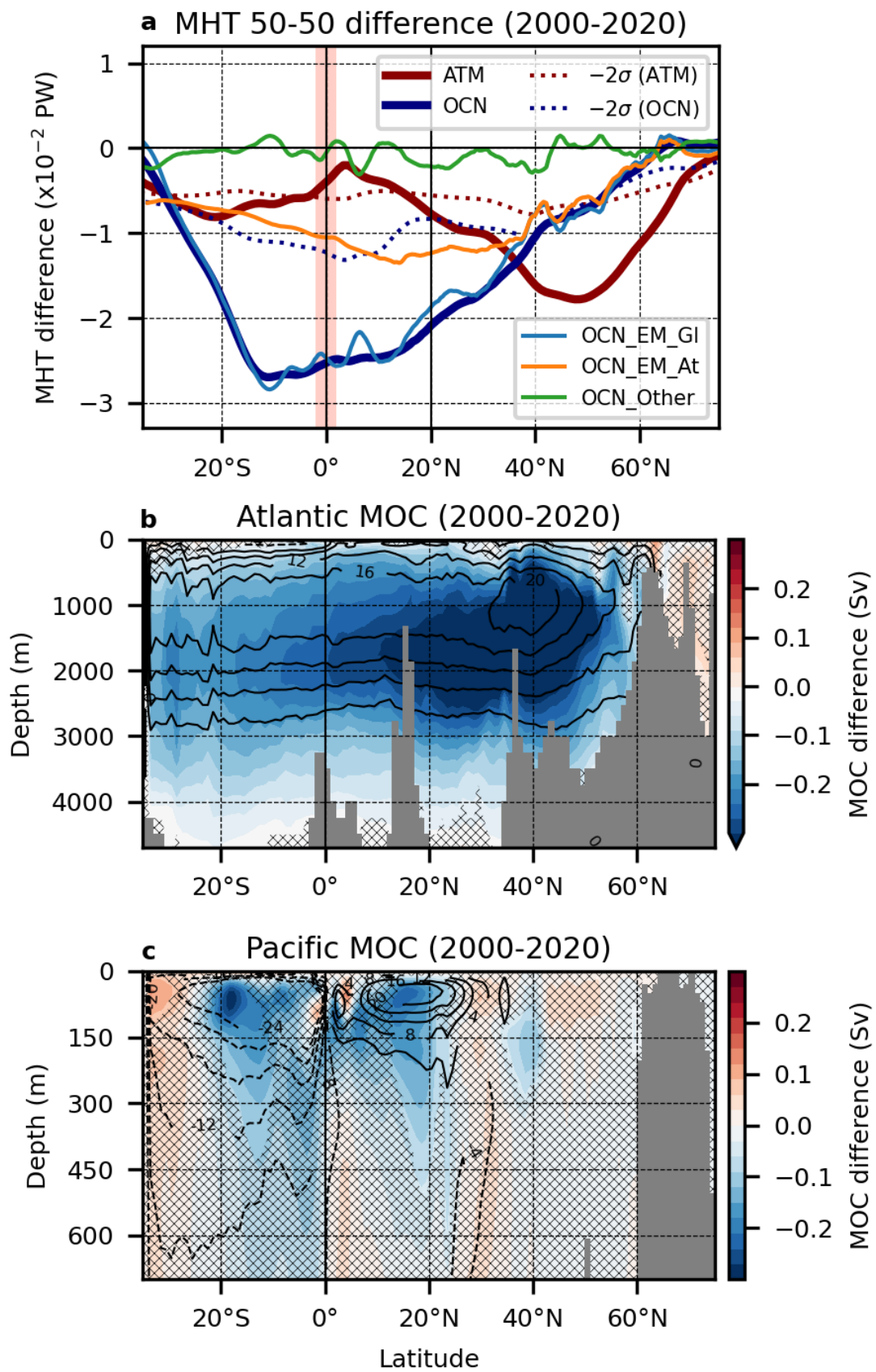
379 *b. Ocean basin response for compensating and/or sequestering the heat*

380 Although for both the North Pacific and the North Atlantic the anomalous heating
381 associated with higher-amplitude variability BBA emissions is compensated by the ensuing
382 OHTC anomalies, the meridional extent of the ocean heat transport anomalies is notably
383 different between the two ocean basins. During the latter half of the high-amplitude BBA
384 emission period (2000–2020) when the OHTC anomalies are large, the global ocean meridional

385 heat transport (MHT) anomalies extend broadly from 60°N to the south of 30°S with the
386 dominant contribution from the Eulerian mean component to its southward anomalies ([Fig. 7a](#)).
387 The MHT anomalies for the North Atlantic Ocean are responsible for a portion of the global
388 ocean MHT anomalies broadly from 60°N to at least 30°S. On the other hand, the negative
389 MHT anomalies in the Indo-Pacific basin, mainly caused by the Eulerian mean component (the
390 difference between OCN_EM_Gl and OCN_EM_At in [Fig. 7a](#)), are confined within 30°S–
391 30°N.

392 The dominant Eulerian mean components in the MHT anomalies in each basin correspond
393 well to changes in the MOC over each basin. The meridionally-uniform Atlantic MHT
394 anomalies share their spatial characteristics with the weakening of the AMOC ([Fig. 7b](#)). On
395 the other hand, in the Pacific the shallow Subtropical Cells (STCs, McCreary and Lu 1994) at
396 low latitudes (30°S–30°N) weaken in the NH and strengthen in the SH during the latter half of
397 the period of the high-amplitude BBA emissions ([Fig. 7c](#)). The combined effect of the STC
398 anomalies in both hemispheres can form an anomalous Cross-Equatorial Cell (CEC) which is
399 comprised by ascending (descending) branches in the NH (SH) and southward (northward)
400 currents in surface (subsurface) waters. Southward surface current anomalies at the equator,
401 corresponding to the upper branch of the CEC, are consistent with the southward MHT
402 anomalies in the Pacific Ocean. These basin contrasts of the MOC responses has been identified
403 as well in previous studies that evaluated the response of climate models to hemispherically
404 asymmetric cooling (e.g., Yu and Pritchard 2019; Kang et al. 2021)

405



407 Fig. 7. Differences in sub-ensemble means between CMIP6 and SMBB for (a) meridional
408 heat transport (MHT) and (b and c) meridional overturning circulation (MOC, positive
409 clockwise). Line colors in (a) are the same as in [Fig. 5](#). 100-member ensemble mean
410 climatology of MOC streamlines (2000–2020, Sv) is superimposed as contours in (b) and
411 (c). Statistically insignificant differences at the 95% confidence level are cross-hatched in (b) and
412 (c).

413

414 1) ATLANTIC

415 From a temporal perspective as well, the North Atlantic OHTC anomalies in [Fig 6e](#) are
416 consistent with the AMOC anomalies. In the sub-ensemble members forced by the high-
417 amplitude variability in BBA emissions (CMIP6 members), the AMOC transport, assessed at
418 the latitude where it is maximum (40°N), is ~0.7 Sv smaller than that in the SMBB sub-
419 ensemble both during the period where CMIP6 and SMBB forcing differ and thereafter ([Fig.](#)
420 [2f](#)). The AMOC anomalies are also largest at 40°N, and extend meridionally across the Atlantic
421 basin from the 2000s to the 2030s, and eventually disappear completely by the 2040s ([Fig. S2](#)).
422 In terms of the heat budget, the AMOC anomalies compensate for the anomalous surface heat
423 input into the North Atlantic by reducing mean northward ocean heat transport (i.e., a
424 southward ocean MHT anomaly is induced).

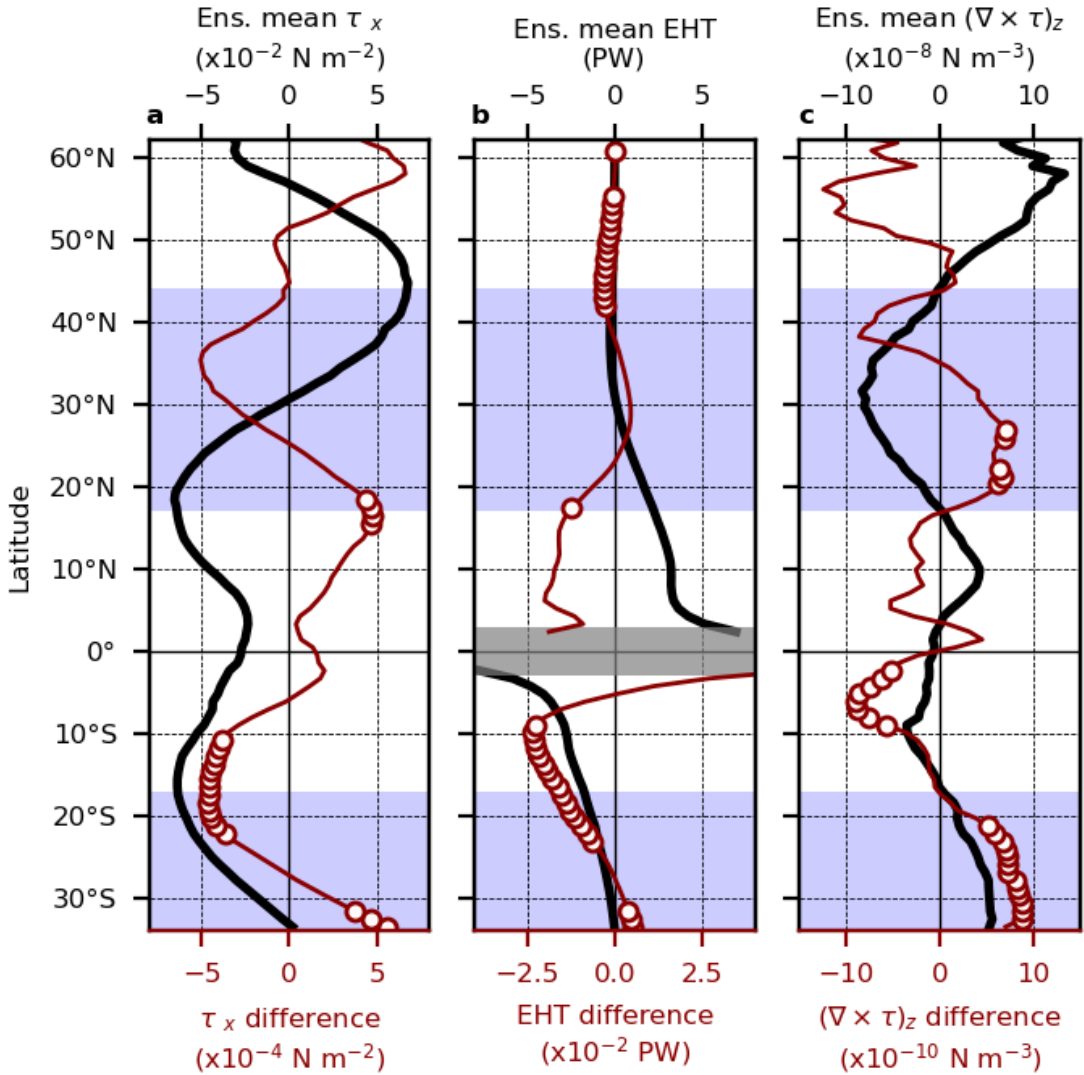
425 The weakening of the AMOC during and after the period of the high-amplitude variability
426 BBA emissions is likely due to the suppression of winter convection ([Fig. S1d](#)) associated with
427 anomalous surface buoyancy gain. On decadal time scales, sea surface buoyancy (freshwater
428 and heat) forcing in the North Atlantic deep convection sites is one of the key factors driving
429 AMOC variability in model simulations (Timmermann et al. 1998; Biastoch et al. 2008; Yeager
430 and Danabasoglu 2014; Pillar et al. 2016). High BBA emissions lead to reduced sea ice
431 formation ([Figs. 2d](#) and [S1f](#)) and thereby a net buoyancy gain due to fresher surface waters to
432 the north of 75°N in the Arctic, while at the same time over 65°N–75°N there is a net buoyancy
433 loss with the decrease in surface freshwater due to the reduced supply of ice ([Figs. S3a](#) and
434 [S3b](#)). However, in the regions where deep convection occurs in this model (the Labrador Sea
435 and the Irminger Sea, [Fig. S1c](#)), the buoyancy gains due to surface heating overcome the
436 freshwater component of the buoyancy flux anomalies ([Fig. S3](#)). As a result, surface buoyancy
437 forcing is positive (buoyancy gain), implying enhanced upper ocean stratification and
438 suppressed winter convection that can lead to a slowdown of the AMOC.

439

440 2) PACIFIC

441 The Pacific STC anomalies (i.e., an anomalous CEC structures) correspond well to zonal
442 wind anomalies, as documented in previous studies with idealized atmosphere-ocean coupled
443 models (Green and Marshall 2017). During the period when CMIP6 and SMBB forcings differ,
444 the trade wind anomalies are largest at the latitudes of their climatological maxima
445 (approximately 18°N and 18°S), with a weakening in the NH and strengthening in the SH (Fig.
446 8a). As a result, meridional Ekman heat transport calculated from the zonal wind stress
447 anomalies and ocean temperature (Sato et al. 2002) show southward anomalies in both the NH
448 and SH, except for latitudes close to and on the equator (Fig. 8b). This is consistent with the
449 MHT anomalies and the zonal mean circulation anomalies seen in Figs. 7a and 7c, respectively.
450 This seems to provide favorable conditions for the anomalous southward ocean CEHT to
451 compensate for the NH decadal warming induced by the BBA emissions difference between
452 CMIP6 and SMBB. Indeed, previous studies (Green and Marshall 2017; Kang et al. 2018) have
453 proposed that mechanistic coupling with changes in the trade winds (i.e., Hadley circulation)
454 could form an ocean CEC through Ekman dynamics, and create ocean CEHT anomalies in the
455 same direction as the atmosphere. In contrast, such a relationship is not apparent in the Atlantic
456 (Fig. S4).

457



458

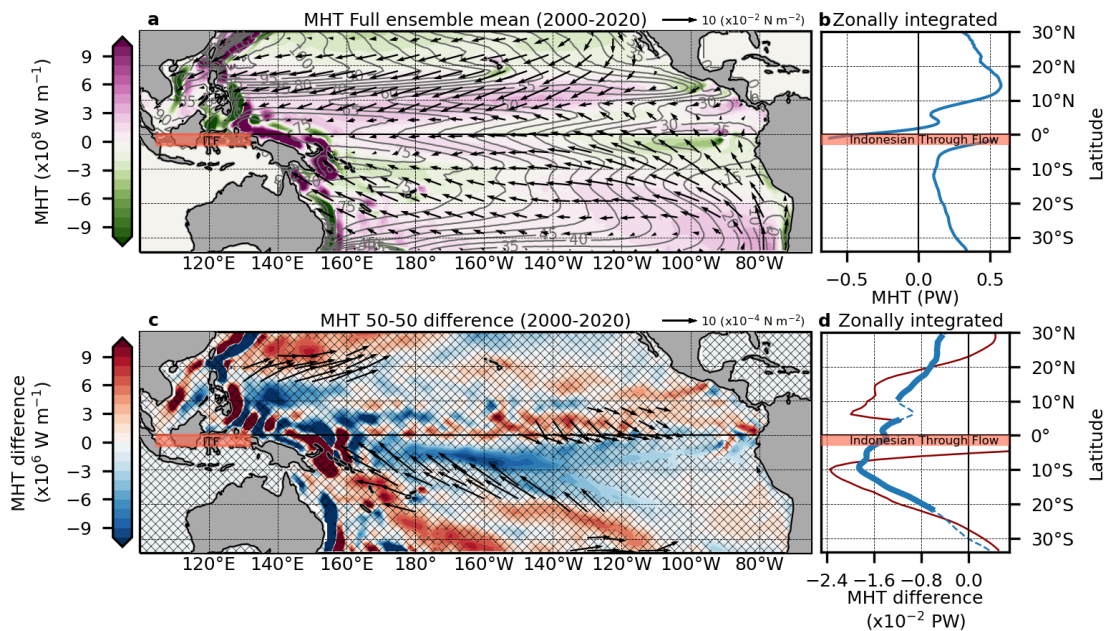
459 Fig. 8. Pacific 100-member ensemble mean climatology (black lines with upper x-axis) and
460 sub-ensemble mean difference (CMIP6 minus SMBB, red lines with bottom x-axis) in (a) zonal
461 mean zonal wind stress (τ_x , positive eastward), (b) zonally integrated meridional Ekman heat
462 transport (EHT, positive northward), and (c) zonal mean surface wind stress curl ($(\nabla \times \tau)_z$).
463 Blue-shaded latitudes represent the subtropics in each hemisphere defined from the zonal mean
464 surface wind stress curl. The white dots on the differences (red lines) indicate statistically
465 significant differences at the 95% confidence level based on the bootstrapping method.

466

467 However, the actual current fields that constitute the Pacific STCs are complicated, and the
468 STCs and the associated MHTs are not fully explained by the near-surface Ekman currents
469 alone that are directly driven by local trade winds. The factors that play a dominant role in the
470 net northward basin-wide (zonally integrated) Pacific MHT reflects a complex interplay
471 between narrow WBCs and broad near-surface currents away from the western boundary (non-
472 WBCs), with the relative contributions being latitude-dependent (Figs. 9a and 9b). Over the

473 latitudes of the North Pacific subtropical gyre (north of 20°N), northward transport by the WBC
 474 (Kuroshio) contributes dominantly to the net northward MHT. In the lower latitudes of the
 475 North Pacific comprising the tropical circulation system, including the southward-flowing
 476 equatorial WBC (Mindanao Current) but excepting the equatorial waveguide region (3°N–3°S),
 477 northward Ekman heat transport in the non-WBC region due to prevailing trade winds forms
 478 the net northward MHT. In the SH, the northward MHT by the northward WBCs of the tropical
 479 circulation system [the New Guinea Coastal Undercurrent (NGCU) and North Queensland
 480 Current/Hiri Current (NQC/HC), cf. Cravatte et al. 2011] is dominant equatorward of 18°S,
 481 while the non-WBC northward heat transport is dominant in the subtropical gyre (at least,
 482 ~34°S as shown in Fig. 9a), resulting in the net northward basin-integrated MHT over all
 483 latitudes for the SH.

484



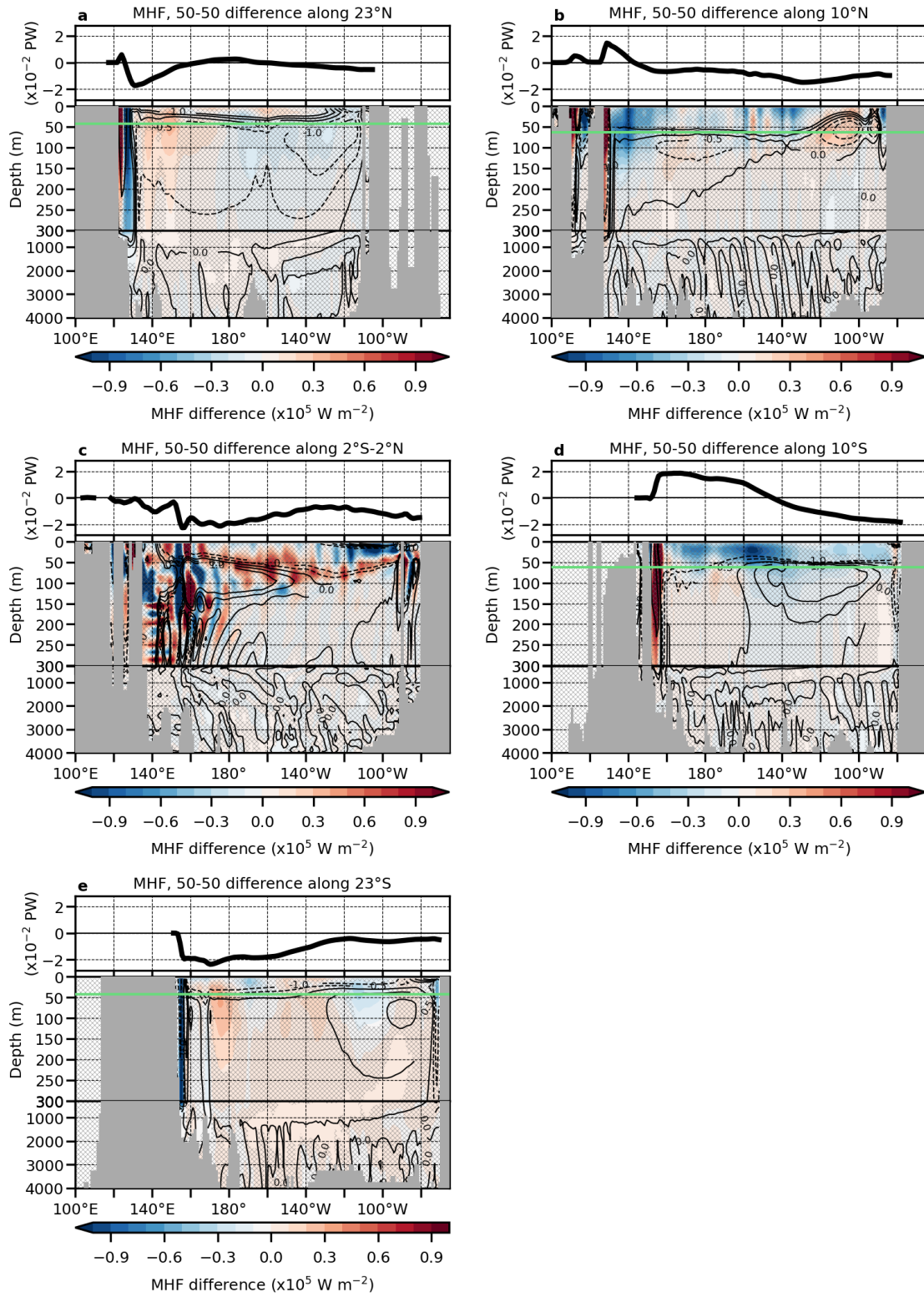
485

486 Fig. 9. (a and b) 100-member ensemble mean climatology (2000–2020) of and (c and d)
 487 sub-ensemble mean difference (CMIP6-SMBB) in ocean full-depth meridional heat transport
 488 (MHT, positive northward), surface wind stress, and zonally integrated ocean MHT. 100-
 489 ensemble mean climatology of SSH (cm) is shown as contours in (a). The 50–50 difference of
 490 the meridional Ekman heat transport (EHT, same as Fig. 8b) are also shown as the red line in
 491 (d). In (c), statistically insignificant MHT differences at the 95% confidence level are cross-
 492 hatched and only wind stress differences for which the zonal components are statistically
 493 significant at the 95% confidence level are shown. Statistically significant zonally integrated
 494 MHT differences are shown as thick solid lines in (d).

495

496 As was the case with the climatological currents, the southward MHT anomalies due to the
497 BBA-induced anomalous Pacific CEC reveal latitude-dependence ([Figs. 9c](#) and [9d](#)). In the
498 North Pacific subtropical gyre (north of 20°N), anomalous ocean meridional heat flux (MHF)
499 by the WBCs is the principal contribution to the Pacific basin's net southward MHT anomalies
500 ([Figs. 10a](#)). The northward MHT by the North Pacific subtropical WBC (the Kuroshio) is
501 weakened, such that the zonally-integrated MHT anomalies are southward over the respective
502 latitudes. On the other hand, over the equatorward portion of the South Pacific subtropical gyre
503 (18°S–30°S), anomalous southward MHF due to a strengthened South Pacific subtropical
504 WBC (the Eastern Australian Current) contributes to the basin-wide southward MHT
505 anomalies over the respective latitudes ([Figs. 10e](#)). These WBC transport changes are driven
506 by anomalies in the surface wind stress curl and its zonal integral ([Fig. 8c](#)). In other words, the
507 North Pacific subtropical gyre weakens and the Southern Pacific subtropical gyre strengthens.

508



509

510 Fig. 10. The difference in CMIP6 and SMBB ensemble means of meridional ocean heat
 511 flux (MHF, positive northward, shadings) along five latitudes [a: 20°N, b: 10°N, c: Equator
 512 (2°S–2°N), d: 10°S, and e: 20°S]. Upper panels on each depth-longitude section show eastward
 513 cumulative sum of depth-integrated MHF 50–50 difference from the western boundary (i.e.,
 514 their values at the eastern boundary are identical to Fig. 9d). Climatological mean (100-

ensemble mean) MHFs (10^6 W m^{-2}) are superimposed in the lower panels as contours [contour levels = ($\pm 100.$, $\pm 10.$, $\pm 1.$, ± 0.5 , $0.$)]. Statistically insignificant MHF differences at the 95% confidence level are cross-hatched. The green lines in the (a), (b), (d), and (e) indicate approximate Ekman layer depth defined as $\sqrt{2A_V/f}$, where A_V and f are the eddy viscosity ($A_V = 0.05 \text{ m}^2 \text{ s}^{-1}$) and the Coriolis parameter, respectively.

520

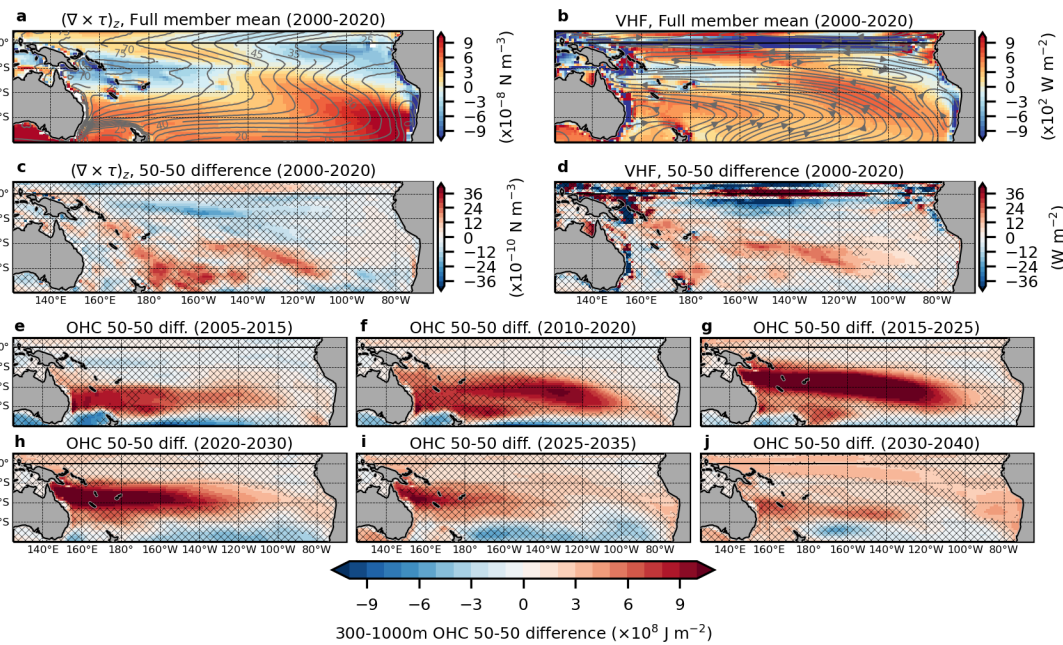
In contrast to the subtropics, over the latitudes associated with the tropical circulation system, MHT anomalies promoted through the Ekman heat transport in non-WBC regions play an important role in generating the net southward Pacific basin MHT anomalies (Fig. 9d). In the North Pacific component of the tropical Pacific circulation (2° – 18°N), reduced northward Ekman heat transport due to weakened trade winds to the east of 130°E contributes to the net southward zonally-integrated MHT anomaly (Fig. 10b). For the South Pacific component of the tropical Pacific circulation (2° – 16°S), the net southward zonally-integrated MHT anomalies are caused by enhanced southward Ekman heat transport due to trade wind strengthening, a characteristic that is widely distributed over the ocean basin at 10°S (Fig. 10d).

At the equator, the response is more complicated. MHT anomalies associated with the enhanced narrow southward current around 155°E mainly contribute to the net southward CEHT anomaly, with secondary contributions from near-surface southward CEHT anomalies east of 130°W (Fig. 10c). This equatorial behavior, which demonstrates a dominant contribution of the frictional WBC to sustain anomalous CEHT at the equator, is more consistent with recent results obtained with a low-resolution idealized atmosphere-ocean coupled model by Green et al. (2019) than it is with the framework whereby the CEHT is sustained by a shifting of the STCs themselves (Schneider 2017). That is to say, from the northern boundary of the anomalous CEC (around 30°N) to the southern boundary (near 30°S), the dominant contributions for generating the net southward MHT anomalies differs between the contributions in WBC regions and non-WBC regions, depending on their latitude.

The strong convergence of the southward zonally-integrated MHT anomalies south of 10°S (Fig. 9d) implies a downward shunting of heat into the ocean interior, thereby accounting for the accumulation of heat in the low-latitude Pacific (Equatorial and South Pacific) already identified in Fig. 6g. For the South Pacific subtropics (from approximately 18°S to 40°S), with the exception of the coastal regions, vertical heat flux (VHF) just below the layer where it interacts directly with the atmosphere (below about 100 m depth) corresponds well to what is expected from the surface wind stress curl ($(\nabla \times \boldsymbol{\tau})_z$) field through Ekman dynamics (Figs. 11a

548 and 11b). During the period when CMIP6 and SMBB forcing is different, differences between
 549 two 50-member sub-ensembles indicates a positive wind stress curl anomaly over the South
 550 Pacific subtropical gyre (Fig. 11c). These positive anomalies enhance the Ekman pumping
 551 (downwelling) and hence induce anomalous VHF that carry more heat into the subsurface
 552 layer (Fig. 11d). The heat transported below 300 m depth accumulates within the South Pacific
 553 subtropical gyre, and through time is advected along a circulation structure extending to
 554 approximately 10°S (Figs. 11e–11g). Part of the heat is then transported to the subsurface zone
 555 of the equatorial band via the northward NQC/HC and NGCU (Figs. 11h–11j). These heat
 556 anomalies accumulated within the South Pacific Subtropical gyre and those reached below the
 557 equatorial thermocline both contribute to the low-latitude Pacific OHC anomalies that persist
 558 until the end of the simulation (Figs. 6g and S5). Over a longer-timescale than is the main focus
 559 of this study, baroclinic wave adjustment associated with an abrupt AMOC change
 560 (Timmermann et al. 2005) can also be expected to induce subsurface temperature anomalies in
 561 the tropical and South Pacific (Wang et al. 2018). Here, however, we emphasize the importance
 562 of the local wind forcing (positive wind stress curl anomalies) in this shorter time-scale ocean
 563 response.

564



565

566 Fig. 11. 100-member ensemble mean climatology (2000–2020) of (a) surface wind stress
 567 curl ($(\nabla \times \tau)_z$) and SSH [contours, (cm)] and (b) 100–300 m mean vertical heat flux (VHF,
 568 positive downward) and streamlines at 300 m depth. Differences in sub-ensemble means
 569 (CMIP6 minus SMBB) in (c) $(\nabla \times \tau)_z$, (d) VHF, and (e–j) subsurface ocean heat content (OHC,

570 300–1000 m). Statistically insignificant differences at the 95% confidence level are cross-
571 hatched in (c–j).

572

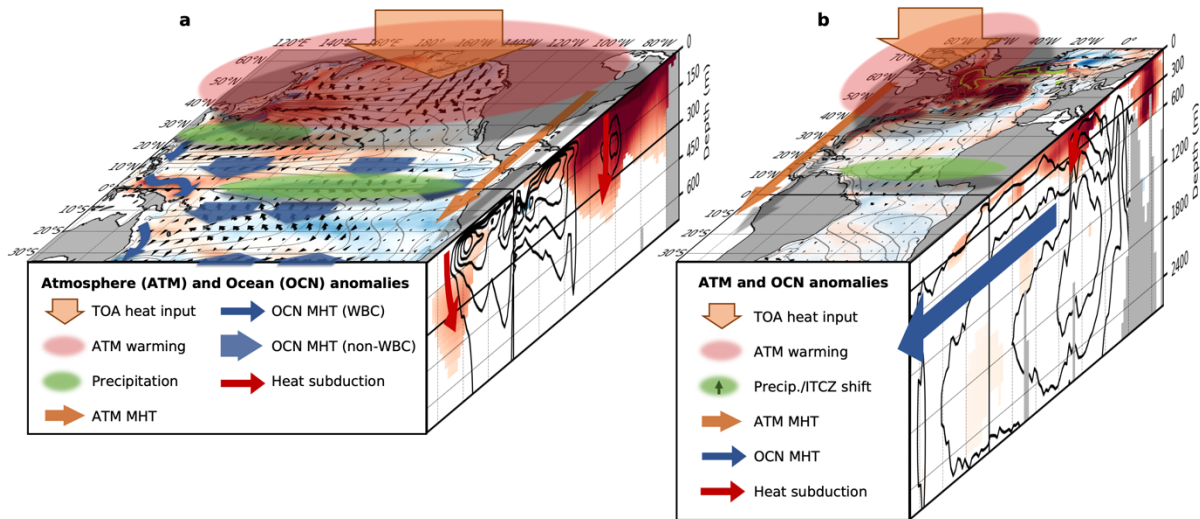
573 **5. Summary and Discussion**

574 We have investigated the ocean response to anomalous NH warming induced by a rectified
575 response to interannual modulations of BBA emissions and corresponding shortwave radiation.
576 We compared two 50-member sub-ensembles of the 100-member CESM2-LE, with their BBA
577 emission forcing differing over 1990–2020. By virtue of having two large sets of simulation
578 with 50 ensemble members in each, which were conducted by a fully coupled Earth system
579 model, our experimental design facilitates a clear separation of the forced response to changes
580 in the interannual variability of BBA emissions from background natural variability. The main
581 takeaways of this study are (1) the detailed description of the complexity of the Pacific CEC
582 response and (2) the explanation of the mechanism for heat accumulation at the Pacific
583 subsurface, resulting in the long-lasting oceanic memory of the interannual BBA forcing. Our
584 emphasis on the ocean response to hemispherically asymmetric thermal forcing, especially in
585 the anomalous Pacific CEC, is complementary to previous more atmospherically-focused
586 studies that have applied atmosphere-slab ocean coupled models (e.g., Manabe and Broccoli
587 1985; Chiang et al. 2003; Kang et al. 2008), and studies with idealized atmosphere-ocean
588 coupled models (e.g., Green and Marshall 2017) , as well as studies applying state-of-the-art
589 climate models with limited numbers of ensemble members (e.g., White et al. 2018; Yu and
590 Pritchard 2019), along with studies that have considered longer-timescale responses (from
591 interdecadal to equilibrium) responses (e.g., Tomas et al. 2016; Wang et al. 2018, 2022).

592 Detectable differences in the responses of the Pacific and Atlantic Oceans are summarized
593 schematically in [Fig. 12](#). The initial atmospheric and sea-ice responses to anomalous heat input
594 through radiation across the top of the atmosphere in the NH high latitudes are common to both
595 basins (e.g., atmospheric warming, increased in atmospheric southward CEHT, and sea ice
596 melting), but the subsequent ocean responses are notably different between the two basins. In
597 the Atlantic, heat absorbed by the ocean warms the upper part of the North Atlantic and
598 enhances upper ocean stratification ([Fig. S6a](#)). Some of the heat is subducted into the
599 subsurface within the subtropical and subpolar gyres ([Fig. S6b](#)) and the enhanced stratification
600 slows the AMOC down. The warm anomalies in the upper North Atlantic Ocean are
601 compensated by the reduction in northward ocean heat transport due to the weakened AMOC

which occurs broadly across the basin. Subsequent to the time interval when forcing is divergent, part of the forced warm anomaly remains in the subsurface for multiple decades (Figs. S6c–S6f), while the ocean continually releases anomalous heat into the atmosphere.

605



606

Fig. 12. Schematic figure for illustrating (a) Pacific and (b) Atlantic Ocean responses to the NH decadal warming induced by the high-amplitude BBA emissions variability. The top panels show differences in sub-ensemble mean (CMIP6 minus SMBB for 2000–2020) net surface heat flux (positive downward) and surface wind as shadings and vectors, respectively. The contours in the top panel indicate 100-member mean SSH. In the side panels, differences in sub-ensemble mean temperature (shadings) and MOC (contours) are shown. Note that only negative MOC anomalies from Fig. 7 are shown as contours.

614

Like the Atlantic, the upper Pacific Ocean is warmed directly during the period when BBA emissions forcing is different (Fig. S5a). In contrast to the Atlantic, however, the anomalous CEC in the Pacific that is induced is associated with hemispherically asymmetric trade wind anomalies, characterized by weakened NH trade winds and strengthened SH trade winds. We found that the anomalous CEC and the resultant net southward ocean MHT anomalies covering the tropical Pacific (30°S–30°N) reflect a complex latitude-dependent interplay between the WBCs and the near-surface Ekman transport away from the western boundary regions. The deceleration of the North Pacific subtropical WBC (Kuroshio), a component of the anomalous CEC, reduces northward heat transport into the North Pacific and thereby to an extent partly compensates for the anomalous heat flux into the North Pacific. Other components of the heat flux perturbation applied across the surface of the North Pacific are subsequently released to the atmosphere and/or transferred into the subsurface (Figs. S5a–S5c). In the South Pacific, the

627 southward heat transport anomalies converge and by this means heat is shunted into the
628 subsurface. Heat accumulated in the subsurface of the South Pacific subtropical circulation is
629 then partly transported to the layer below the equatorial thermocline via the NGCU, which
630 contributes to the persistent ocean memory (Figs. S5d–S5f).

631 The primary factors distinguishing the ocean responses between the Pacific and Atlantic
632 are the presence of a deep MOC structure for the Atlantic relative to the Pacific, and the
633 enhanced efficiency for the Pacific of zonally-integrated wind stress curl-driven transport
634 anomalies, as a consequence of the significantly broader zonal extent. For the present case, the
635 anomalous increase in OHC is smaller in the Atlantic than in the Pacific, even though the
636 Atlantic gains 30% more heat through local heat flux anomalies during the period of the high-
637 amplitude BBA emissions variability (Fig. S7). For the Atlantic, the AMOC is able to
638 compensate NH warming anomalies by virtue of not only its access to a deep heat reservoir but
639 also the broad meridional reach of its coherent circulation pattern, meaning that there is more
640 direct leverage for an anomalous OHTC reduction through its southern end (Fig. S7). As the
641 Pacific is a much wider basin than the Atlantic, net CEC anomalies can be more effectively
642 controlled by anomalies in trade wind strength associated with hemispherically asymmetric
643 thermal forcing perturbations.

644 This study has broader implications for understanding the response of the climate system
645 to BBA emissions. As has been described above, previous studies (Fasullo et al. 2022;
646 DeRepentigny et al. 2022; Kim et al. *under review*) have shown that the BBA emissions forcing
647 protocols for CMIP6 (BB4CMIP6), with spurious discontinuities in the variance of BBA
648 emissions, are somewhat of a mixed blessing. Despite the increased realism in this forcing
649 during data-rich periods, spurious changes in the amplitude of BBA emissions can lead to
650 spurious mean state changes in a number of important climate variables. Viewing this in a
651 positive light, this sensitivity to large changes in the variance of BBA emissions has also drawn
652 our attention to a previously under-appreciated role for BBA emissions in the climate system.

653 Moving forward, there are two points that we wish to emphasize that are informed by what
654 we have learned thus far. First, the rectified heat anomalies in the atmosphere associated with
655 changes in the interannual variability of BBA emissions are only an order of 0.4 W m^{-2} , and
656 yet this is sufficient to trigger large-scale adjustment processes reaching into the SH. It is
657 valuable to consider this within the context of volcanic eruptions (Church et al. 2005;
658 Stenchikov et al. 2009) where the short-term intensity of forcing from an individual volcano

659 can be ten times larger in magnitude ($\sim -4 \text{ W m}^{-2}$ vs. $\sim 0.4 \text{ W m}^{-2}$ of TOA radiation anomalies),
660 but where the net the Earth system perturbation can be of similar amplitude [maximum global
661 OHC anomaly of $\sim 50 \text{ ZJ}$ for a Pinatubo-level volcanic eruption (Stenchikov et al. 2009)
662 compared to $\sim 20 \text{ ZJ}$ for increased interannual BBA variability in this study]. Although
663 individual TOA anomalies associated with high-amplitude modulations of BBA emissions
664 variability are smaller, the cumulative impact of intermittent anomalies can have impacts on
665 the system comparable to those of a large volcanic eruption event.

666 Second, the fact that the forcing perturbation of CMIP6-SMBB over 1990–2020 spans only
667 12% of the full 251 years of the CESM2-LE (1850-2100) implies that if realistic BBA
668 emissions were used over the full 1850-2100 period, one might expect that the cumulative
669 ocean heat response to the forcing could be larger than it is under SMBB forcing perturbation
670 considered here. This could be particularly pertinent if interannual variability in BBA
671 emissions were to increase in time with climate change (e.g., van der Werf et al. 2017). With
672 this in mind, it is recommended that the work presented here be extended by considering the
673 climate feedbacks associated with realistic modulations of the frequency and/or intensity of
674 fire occurrence over scenario runs spanning 1850-2100. Such an effort would benefit not only
675 our understanding of the processes that contribute to climate change, but also the development
676 of new protocols that can be applied to the CMIP7 modeling project.
677

678 *Acknowledgments.*

679 This study was supported by the Institute for Basic Science (IBS), Republic of Korea, under
680 IBS-R028-D1. This material is based upon work supported by the National Center for
681 Atmospheric Research, which is a major facility sponsored by the NSF under Cooperative
682 Agreement 1852977. MFS was supported by NSF grant AGS-2141728 and NOAA's Climate
683 Program Office's Modeling, Analysis, Predictions, and Projections (MAPP) program grant
684 NA20OAR4310445. This is IPRC publication X and SOEST contribution Y. The CESM2
685 simulations were conducted on the IBS/ICCP supercomputer ‘Aleph’, 1.43 peta flops high-
686 performance Cray XC50-LC Skylake computing system with 18,720 processor cores, 9.59 PB
687 storage and 43 PB tape archive space. We also acknowledge the support of KREONET.
688

689 *Data Availability Statement.*

The CESM2-LE data is available through NCAR's Climate Data Gateway at
<https://www.earthsystemgrid.org/dataset/ucar.cgd.cesm2le.output.html>.

692

693 REFERENCES

- 694 Archibald, S., C. E. R. Lehmann, J. L. Gómez-Dans, and R. A. Bradstock, 2013: Defining
695 pyromes and global syndromes of fire regimes. *Proceedings of the National Academy of*
696 *Sciences*, **110**, 6442–6447, <https://doi.org/10.1073/pnas.1211466110>.

697 Biastoch, A., C. W. Böning, J. Getzlaff, J.-M. Molines, and G. Madec, 2008: Causes of
698 Interannual-Decadal Variability in the Meridional Overturning Circulation of the
699 Midlatitude North Atlantic Ocean. *Journal of Climate*, **21**, 6599–6615,
700 <https://doi.org/10.1175/2008JCLI2404.1>.

701 Bogenschutz, P. A., A. Gettelman, C. Hannay, V. E. Larson, R. B. Neale, C. Craig, and C.-C.
702 Chen, 2018: The path to CAM6: coupled simulations with CAM5.4 and CAM5.5.
703 *Geoscientific Model Development*, **11**, 235–255, <https://doi.org/10.5194/gmd-11-235-2018>.

704 Broccoli, A. J., K. A. Dahl, and R. J. Stouffer, 2006: Response of the ITCZ to Northern
705 Hemisphere cooling. *Geophysical Research Letters*, **33**,
706 <https://doi.org/10.1029/2005GL024546>.

707 Chiang, J. C. H., and A. R. Friedman, 2012: Extratropical Cooling, Interhemispheric Thermal
708 Gradients, and Tropical Climate Change. *Annu. Rev. Earth Planet. Sci.*, **40**, 383–412,
709 <https://doi.org/10.1146/annurev-earth-042711-105545>.

710 Chiang, J. C. H., M. Biasutti, and D. S. Battisti, 2003: Sensitivity of the Atlantic Intertropical
711 Convergence Zone to Last Glacial Maximum boundary conditions. *Paleoceanography*,
712 **18**, <https://doi.org/10.1029/2003PA000916>.

713 Church, J. A., N. J. White, and J. M. Arblaster, 2005: Significant decadal-scale impact of
714 volcanic eruptions on sea level and ocean heat content. *Nature*, **438**, 74–77,
715 <https://doi.org/10.1038/nature04237>.

716 Cravatte, S., A. Ganachaud, Q.-P. Duong, W. S. Kessler, G. Eldin, and P. Dutrieux, 2011:
717 Observed circulation in the Solomon Sea from SADCP data. *Progress in Oceanography*,
718 **88**, 116–130, <https://doi.org/10.1016/j.pocean.2010.12.015>.

719

- 720 Danabasoglu, G., S. C. Bates, B. P. Briegleb, S. R. Jayne, M. Jochum, W. G. Large, S.
721 Peacock, and S. G. Yeager, 2012: The CCSM4 Ocean Component. *J. Climate*, **25**, 1361–
722 1389, <https://doi.org/10.1175/JCLI-D-11-00091.1>.
- 723 Danabasoglu, G., and Coauthors, 2020: The Community Earth System Model Version 2
724 (CESM2). *Journal of Advances in Modeling Earth Systems*, **12**, e2019MS001916,
725 <https://doi.org/10.1029/2019MS001916>.
- 726 DeRepentigny, P., and Coauthors, 2022: Enhanced simulated early 21st century Arctic sea ice
727 loss due to CMIP6 biomass burning emissions. *Science Advances*, **8**, eabo2405,
728 <https://doi.org/10.1126/sciadv.abo2405>.
- 729 Deser, C., R. A. Tomas, and L. Sun, 2015: The Role of Ocean–Atmosphere Coupling in the
730 Zonal-Mean Atmospheric Response to Arctic Sea Ice Loss. *Journal of Climate*, **28**, 2168–
731 2186, <https://doi.org/10.1175/JCLI-D-14-00325.1>.
- 732 Eyring, V., S. Bony, G. A. Meehl, C. A. Senior, B. Stevens, R. J. Stouffer, and K. E. Taylor,
733 2016: Overview of the Coupled Model Intercomparison Project Phase 6 (CMIP6)
734 experimental design and organization. *Geosci. Model Dev.*, **9**, 1937–1958,
735 <https://doi.org/10.5194/gmd-9-1937-2016>.
- 736 Fasullo, J. T., J.-F. Lamarque, C. Hannay, N. Rosenbloom, S. Tilmes, P. DeRepentigny, A.
737 Jahn, and C. Deser, 2022: Spurious Late Historical-Era Warming in CESM2 Driven by
738 Prescribed Biomass Burning Emissions. *Geophysical Research Letters*, **49**,
739 e2021GL097420, <https://doi.org/10.1029/2021GL097420>.
- 740 Green, B., and J. Marshall, 2017: Coupling of Trade Winds with Ocean Circulation Damps
741 ITCZ Shifts. *Journal of Climate*, **30**, 4395–4411, <https://doi.org/10.1175/JCLI-D-16-0818.1>.
- 743 —, —, and J.-M. Campin, 2019: The ‘sticky’ ITCZ: ocean-moderated ITCZ shifts. *Clim
744 Dyn*, **53**, 1–19, <https://doi.org/10.1007/s00382-019-04623-5>.
- 745 Hawcroft, M., J. M. Haywood, M. Collins, and A. Jones, 2018: The contrasting climate
746 response to tropical and extratropical energy perturbations. *Clim Dyn*, **51**, 3231–3249,
747 <https://doi.org/10.1007/s00382-018-4076-8>.
- 748 Heyblom, K. B., H. A. Singh, P. J. Rasch, and P. DeRepentigny, 2022: Increased Variability
749 of Biomass Burning Emissions in CMIP6 Amplifies Hydrologic Cycle in the CESM2

- 750 Large Ensemble. *Geophysical Research Letters*, **49**, e2021GL096868,
751 <https://doi.org/10.1029/2021GL096868>.
- 752 Hunke, E. C., W. H. Lipscomb, A. K. Turner, N. Jeffery, and S. Elliott, 2015: CICE: the Los
753 Alamos Sea Ice Model Documentation and Software User's Manual Version 5. 116,
754 <http://www.ccpo.odu.edu/~klinck/Reprints/PDF/cicedoc2015.pdf>.
- 755 Kang, S. M., 2020: Extratropical Influence on the Tropical Rainfall Distribution. *Curr Clim
756 Change Rep*, **6**, 24–36, <https://doi.org/10.1007/s40641-020-00154-y>.
- 757 ——, I. M. Held, D. M. W. Frierson, and M. Zhao, 2008: The Response of the ITCZ to
758 Extratropical Thermal Forcing: Idealized Slab-Ocean Experiments with a GCM. *Journal
759 of Climate*, **21**, 3521–3532, <https://doi.org/10.1175/2007JCLI2146.1>.
- 760 ——, Y. Shin, and S.-P. Xie, 2018: Extratropical forcing and tropical rainfall distribution:
761 energetics framework and ocean Ekman advection. *npj Clim Atmos Sci*, **1**, 1–10,
762 <https://doi.org/10.1038/s41612-017-0004-6>.
- 763 ——, S.-P. Xie, C. Deser, and B. Xiang, 2021: Zonal mean and shift modes of historical
764 climate response to evolving aerosol distribution. *Science Bulletin*, **66**, 2405–2411,
765 <https://doi.org/10.1016/j.scib.2021.07.013>.
- 766 Lamarque, J.-F., and Coauthors, 2010: Historical (1850–2000) gridded anthropogenic and
767 biomass burning emissions of reactive gases and aerosols: methodology and application.
768 *Atmospheric Chemistry and Physics*, **10**, 7017–7039, <https://doi.org/10.5194/acp-10-7017-2010>.
- 770 Lawrence, D. M., and Coauthors, 2019: The Community Land Model Version 5: Description
771 of New Features, Benchmarking, and Impact of Forcing Uncertainty. *Journal of Advances
772 in Modeling Earth Systems*, **11**, 4245–4287, <https://doi.org/10.1029/2018MS001583>.
- 773 Manabe, S., and A. J. Broccoli, 1985: The influence of continental ice sheets on the climate
774 of an ice age. *Journal of Geophysical Research: Atmospheres*, **90**, 2167–2190,
775 <https://doi.org/10.1029/JD090iD01p02167>.
- 776 van Marle, M. J. E., and Coauthors, 2017: Historic global biomass burning emissions for
777 CMIP6 (BB4CMIP) based on merging satellite observations with proxies and fire models
778 (1750–2015). *Geosci. Model Dev.*, **10**, 3329–3357, <https://doi.org/10.5194/gmd-10-3329-2017>.

- 780 McCrae, J. P., and P. Lu, 1994: Interaction between the Subtropical and Equatorial Ocean
781 Circulations: The Subtropical Cell. *Journal of Physical Oceanography*, **24**, 466–497,
782 [https://doi.org/10.1175/1520-0485\(1994\)024<0466:IBTSAE>2.0.CO;2](https://doi.org/10.1175/1520-0485(1994)024<0466:IBTSAE>2.0.CO;2).
- 783 Pillar, H. R., P. Heimbach, H. L. Johnson, and D. P. Marshall, 2016: Dynamical Attribution
784 of Recent Variability in Atlantic Overturning. *Journal of Climate*, **29**, 3339–3352,
785 <https://doi.org/10.1175/JCLI-D-15-0727.1>.
- 786 Rabin, S. S., and Coauthors, 2017: The Fire Modeling Intercomparison Project (FireMIP),
787 phase 1: experimental and analytical protocols with detailed model descriptions. *Geosci.
788 Model Dev.*, **10**, 1175–1197, <https://doi.org/10.5194/gmd-10-1175-2017>.
- 789 Rodgers, K. B., and Coauthors, 2021: Ubiquity of human-induced changes in climate
790 variability. *Earth System Dynamics*, **12**, 1393–1411, <https://doi.org/10.5194/esd-12-1393-2021>.
- 792 Sato, O. T., P. S. Polito, and W. Timothy Liu, 2002: Intra-decadal variability in the Ekman
793 heat flux from scatterometer winds: INTRA-DECADAL VARIABILITY IN THE
794 EKMAN HEAT FLUX. *Geophys. Res. Lett.*, **29**, 12-1-12-14,
795 <https://doi.org/10.1029/2002GL014775>.
- 796 Schneider, T., 2017: Feedback of Atmosphere-Ocean Coupling on Shifts of the Intertropical
797 Convergence Zone. *Geophysical Research Letters*, **44**, 11,644–11,653,
798 <https://doi.org/10.1002/2017GL075817>.
- 799 ——, T. Bischoff, and G. H. Haug, 2014: Migrations and dynamics of the intertropical
800 convergence zone. *Nature*, **513**, 45–53, <https://doi.org/10.1038/nature13636>.
- 801 Smith, R., and Coauthors, 2010: The Parallel Ocean Program (POP) reference manual: Ocean
802 component of the Community Climate System Model (CCSM).
803 <http://n2t.net/ark:/85065/d70g3j4h>.
- 804 Stenchikov, G., T. L. Delworth, V. Ramaswamy, R. J. Stouffer, A. Wittenberg, and F. Zeng,
805 2009: Volcanic signals in oceans. *Journal of Geophysical Research: Atmospheres*, **114**,
806 <https://doi.org/10.1029/2008JD011673>.
- 807 Timmermann, A., M. Latif, R. Voss, and A. Grötzner, 1998: Northern Hemispheric
808 Interdecadal Variability: A Coupled Air–Sea Mode. *Journal of Climate*, **11**, 1906–1931,
809 [https://doi.org/10.1175/1520-0442\(1998\)011<1906:NHIVAC>2.0.CO;2](https://doi.org/10.1175/1520-0442(1998)011<1906:NHIVAC>2.0.CO;2).

- 810 ——, S.-I. An, U. Krebs, and H. Goosse, 2005: ENSO Suppression due to Weakening of the
811 North Atlantic Thermohaline Circulation. *Journal of Climate*, **18**, 3122–3139,
812 <https://doi.org/10.1175/JCLI3495.1>.
- 813 Tomas, R. A., C. Deser, and L. Sun, 2016: The Role of Ocean Heat Transport in the Global
814 Climate Response to Projected Arctic Sea Ice Loss. *Journal of Climate*, **29**, 6841–6859,
815 <https://doi.org/10.1175/JCLI-D-15-0651.1>.
- 816 Wang, K., C. Deser, L. Sun, and R. A. Tomas, 2018: Fast Response of the Tropics to an
817 Abrupt Loss of Arctic Sea Ice via Ocean Dynamics. *Geophysical Research Letters*, **45**,
818 4264–4272, <https://doi.org/10.1029/2018GL077325>.
- 819 ——, L. Wu, H. Liu, B. Dan, H. Dai, and C. Deser, 2022: Contrary Responses of the Gulf
820 Stream and the Kuroshio to Arctic Sea Ice Loss. *Atmosphere*, **13**, 514,
821 <https://doi.org/10.3390/atmos13040514>.
- 822 van der Werf, G. R., and Coauthors, 2017: Global fire emissions estimates during 1997–
823 2016. *Earth System Science Data*, **9**, 697–720, <https://doi.org/10.5194/essd-9-697-2017>.
- 824 White, R. H., A. A. McFarlane, D. M. W. Frierson, S. M. Kang, Y. Shin, and M. Friedman,
825 2018: Tropical Precipitation and Cross-Equatorial Heat Transport in Response to
826 Localized Heating: Basin and Hemisphere Dependence. *Geophysical Research Letters*,
827 **45**, 11,949–11,958, <https://doi.org/10.1029/2018GL078781>.
- 828 Yeager, S., and G. Danabasoglu, 2014: The Origins of Late-Twentieth-Century Variations in
829 the Large-Scale North Atlantic Circulation. *Journal of Climate*, **27**, 3222–3247,
830 <https://doi.org/10.1175/JCLI-D-13-00125.1>.
- 831 Yoshimori, M., A. Abe-Ouchi, H. Tatebe, T. Nozawa, and A. Oka, 2018: The Importance of
832 Ocean Dynamical Feedback for Understanding the Impact of Mid–High-Latitude
833 Warming on Tropical Precipitation Change. *Journal of Climate*, **31**, 2417–2434,
834 <https://doi.org/10.1175/JCLI-D-17-0402.1>.
- 835 Yu, S., and M. S. Pritchard, 2019: A Strong Role for the AMOC in Partitioning Global
836 Energy Transport and Shifting ITCZ Position in Response to Latitudinally Discrete Solar
837 Forcing in CESM1.2. *Journal of Climate*, **32**, 2207–2226, <https://doi.org/10.1175/JCLI-D-18-0360.1>.
- 839